Article

Cell

Noninvasive Deep Brain Stimulation via Temporally Interfering Electric Fields

Graphical Abstract

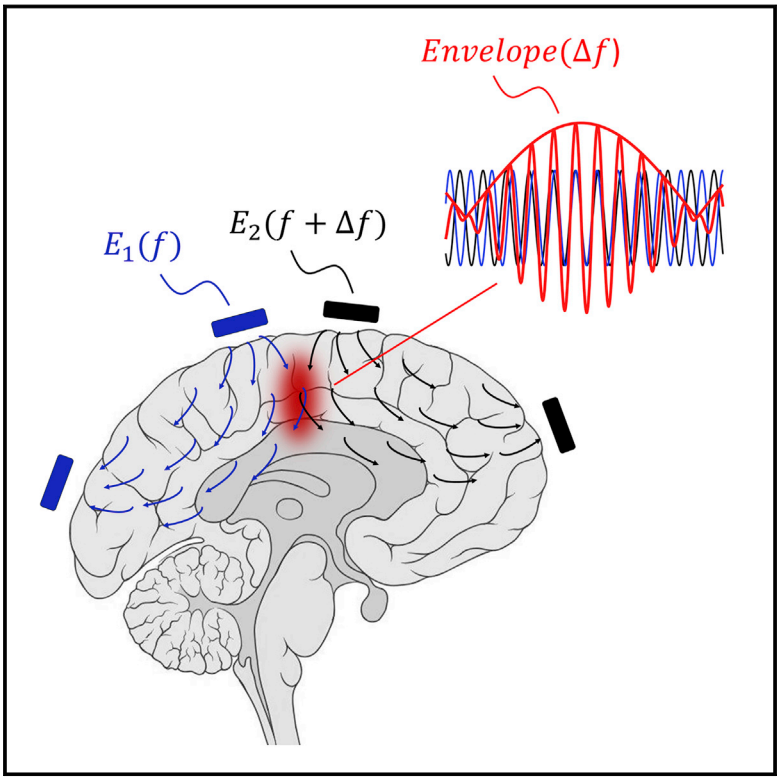

Authors

Nir Grossman, David Bono, Nina Dedic, ..., Li-Huei Tsai, Alvaro Pascual-Leone, Edward S. Boyden

Correspondence

esb@media.mit.edu

In Brief

A noninvasive method for deep-brain stimulation may be a new approach for the treatment of neuropsychiatric diseases.

Highlights

- Noninvasive TI stimulation electrically stimulates neurons at depth selectively
- Neurons are stimulated by interference between multiple electric fields
- Neurons in mouse hippocampus can be stimulated without affecting the overlying cortex

Grossman et al., 2017, Cell *169*, 1029–1041
June 1, 2017
http://dx.doi.org/10.1016/j.cell.2017.05.024

CellPress

Cell, Volume *169*

Supplemental Information

Noninvasive Deep Brain Stimulation via Temporally Interfering Electric Fields

Nir Grossman, David Bono, Nina Dedic, Suhasa B. Kodandaramaiah, Andrii Rudenko, Ho-Jun Suk, Antonino M. Cassara, Esra Neufeld, Niels Kuster, Li-Huei Tsai, Alvaro Pascual-Leone, and Edward S. Boyden

Facilitation and restoration of cognitive function in primate prefrontal cortex by a neuroprosthesis that utilizes minicolumn-specific neural firing

2012 J. Neural Eng. 9 056012

(http://iopscience.iop.org/1741-2552/9/5/056012)

frontiers in Molecular Neuroscience

REVIEW
published: 01 November 2016
doi: 10.3389/fnmol.2016.00108

Non-Viral Nucleic Acid Delivery Strategies to the Central Nervous System

*James-Kevin Y. Tan[1], Drew L. Sellers[1], Binhan Pham[1], Suzie H. Pun[1] and Philip J. Horner[2]**

[1] Department of Bioengineering and Molecular Engineering & Sciences Institute, University of Washington, Seattle, WA, USA,
[2] Center for Neuroregenerative Medicine, Houston Methodist Research Institute, Houston, TX, USA

With an increased prevalence and understanding of central nervous system (CNS) injuries and neurological disorders, nucleic acid therapies are gaining promise as a way to regenerate lost neurons or halt disease progression. While more viral vectors have been used clinically as tools for gene delivery, non-viral vectors are gaining interest due to lower safety concerns and the ability to deliver all types of nucleic acids. Nevertheless, there are still a number of barriers to nucleic acid delivery. In this focused review, we explore the *in vivo* challenges hindering non-viral nucleic acid delivery to the CNS and the strategies and vehicles used to overcome them. Advantages and disadvantages of different routes of administration including: systemic injection, cerebrospinal fluid injection, intraparenchymal injection and peripheral administration are discussed. Non-viral vehicles and treatment strategies that have overcome delivery barriers and demonstrated *in vivo* gene transfer to the CNS are presented. These approaches can be used as guidelines in developing synthetic gene delivery vectors for CNS applications and will ultimately bring non-viral vectors closer to clinical application.

Keywords: central nervous system, delivery, *in vivo*, non-viral, nucleic acid

OPEN ACCESS

Edited by:
George Smith, Temple University School of Medicine, USA

Reviewed by:
Eduardo Fernandez, Universidad Miguel Hernández de Elche, Spain
Marianna Foldvari, University of Waterloo, Canada

***Correspondence:**
Philip J. Horner
pjhorner@houstonmethodist.org

Received: *13 July 2016*
Accepted: *11 October 2016*
Published: *01 November 2016*

Citation:
Tan J-KY, Sellers DL, Pham B, Pun SH and Horner PJ (2016) Non-Viral Nucleic Acid Delivery Strategies to the Central Nervous System. Front. Mol. Neurosci. 9:108. doi: 10.3389/fnmol.2016.00108

INTRODUCTION

The incidence of neurological diseases and injuries is increasing with the rising life expectancy (Mattson and Magnus, 2006). Nucleic acid therapeutics, such as genes and small interfering RNA (siRNA) oligonucleotides have emerged as a promising treatment strategy to preserve neuron function, enhance neurogenesis and prevent the progression of neurological diseases. The delivery of nucleic acids encoding brain-derived neurotrophic factor (Huang et al., 2012a), epidermal growth factor (Sugiura et al., 2005), fibroblast growth factor-2 (Matsuoka et al., 2003), Huntingtin (Burgess et al., 2012), neurogenin-2 (Zhang et al., 2013; Masserdotti et al., 2015), insulin growth factor-1 (Kaspar et al., 2003), and vascular endothelial growth factor (Dodge et al., 2010) have been shown to increase neuron regeneration or delay the progression of neurological diseases in mice, rats and gerbils. Targeting gene delivery vehicles to the appropriate cells and proper protein regulation remain the primary challenges to making these pathways feasible. While viral vectors such as the adeno-associated virus have typically been used clinically, interest in non-viral nucleic acid delivery remains high due to lower safety concerns, greater customizability and an ease in manufacturing (Pack et al., 2005; Burke et al., 2013). In fact, the number of synthetic vectors used in gene therapy clinical trials has been steadily increasing over the last 10 years (Gene Therapy Clinical Trials Worldwide, Wiley).

Resource

Cell

Mapping the Neural Substrates of Behavior

Graphical Abstract

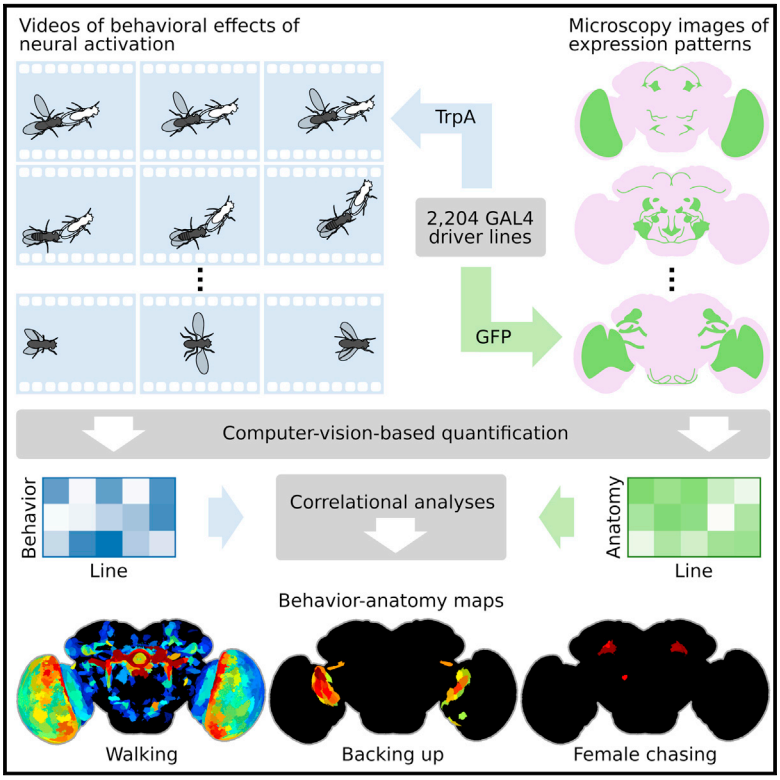

Highlights

- We developed machine-vision methods to broadly and precisely quantify fly behavior
- We measured effects of activating 2,204 genetically targeted neuronal populations
- We created whole-brain maps of neural substrates of locomotor and social behaviors
- We created resources for exploring our results and enabling further investigation

Authors

Alice A. Robie, Jonathan Hirokawa, Austin W. Edwards, ..., Julie H. Simpson, Michael B. Reiser, Kristin Branson

Correspondence

bransonk@janelia.hhmi.org

In Brief

Machine-vision analyses of large behavior and neuroanatomy data reveal whole-brain maps of regions associated with numerous complex behaviors.

Robie et al., 2017, Cell *170*, 393–406
July 13, 2017
http://dx.doi.org/10.1016/j.cell.2017.06.032

CellPress

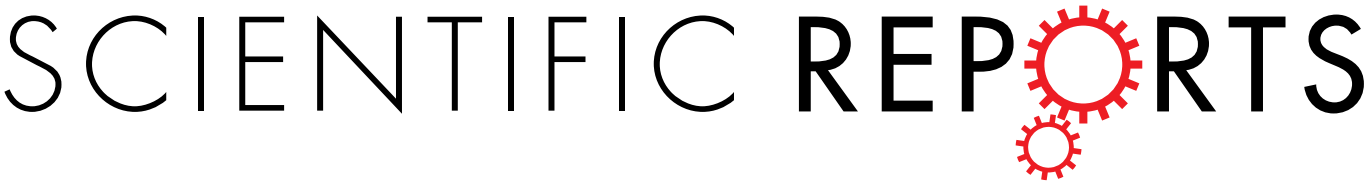

OPEN

Four-pole galvanic vestibular stimulation causes body sway about three axes

Received: 22 July 2014
Accepted: 01 April 2015
Published: 11 May 2015

Kazuma Aoyama[1,2], Hiroyuki Iizuka[3], Hideyuki Ando[1,4] & Taro Maeda[1,4]

Galvanic vestibular stimulation (GVS) can be applied to induce the feeling of directional virtual head motion by stimulating the vestibular organs electrically. Conventional studies used a two-pole GVS, in which electrodes are placed behind each ear, or a three-pole GVS, in which an additional electrode is placed on the forehead. These stimulation methods can be used to induce virtual head roll and pitch motions when a subject is looking upright. Here, we proved our hypothesis that there are current paths between the forehead and mastoids in the head and show that our invented GVS system using four electrodes succeeded in inducing directional virtual head motion around three perpendicular axes containing yaw rotation by applying different current patterns. Our novel method produced subjective virtual head yaw motions and evoked yaw rotational body sway in participants. These results support the existence of three isolated current paths located between the mastoids, and between the left and right mastoids and the forehead. Our findings show that by using these current paths, the generation of an additional virtual head yaw motion is possible.

Since Alessandro Volta invented the battery, it was known that electric current passing through electrodes located between and behind the ears could upset balance and cause a strange sensation in the vestibular system. Nowadays, this electric stimulation is called galvanic vestibular stimulation (GVS) and is mainly used for medical purposes[1,2]; however, this technology can also be applied to virtual reality for engineering purposes. GVS can evoke virtual head motion and sway to the anodal direction by stimulating the vestibular organs electrically[3–5]. Conventional studies used a two-pole GVS in which electrodes are placed behind each ear, or a three-pole GVS in which an additional electrode is placed on the forehead. These stimulation methods can evoke roll and pitch directional sway when a subject is looking upright[6–8]. These studies have shown that the electric current between the mastoids, i.e. two-pole GVS, evokes virtual roll head motion when a subject is looking upright and yaw rotation when a subject is looking down[9]. These sensations occur because the trans-mastoid stimulation brings the virtual head motion about the axis backwards and upwards 18° above the line, joining the lower orbital margin and the external auditory meatus[10–12] (Fig. 1A,B). The stimulation creates a potential gradient from one pole to the other. The three-pole GVS causes virtual head pitch motion and people sway back and forth[6]. This stimulation method is similar to the two-pole stimulation in the sense that the potential gradient is generated from the forehead to the mastoids or vice versa by equating the potentials at the mastoids.

The conventional evidence of two-pole and three-pole GVS indicate that the stimulation current uses paths to pass via the vestibular organs through the head, including between the left and right mastoids or between the forehead and left/right mastoids in order to generate roll (left/right) or pitch (front/back)

[1]Graduate School of Information Science and Technology, Osaka University, 2-1 Yamadaoka, Suita, Osaka, 565-0871, Japan. [2]Japan Society for the Promotion of Science Research Fellowship for Young Scientists (DC1), 5-3-1 Kohjimachi, Chiyoda-ku, Tokyo, Japan. [3]Graduate School of Information Science and Technology, Hokkaido University, Nishi 9-Chome, Kita 14-Jo, Kita-ku, Sapporo, Hokkaido, 060-0814, Japan. [4]Center for Information and Neural Networks (CiNet), National Institute of Information and Communication Technology, 1-4 Yamadaoka, Suita, Osaka, 565-0871, Japan. Correspondence and requests for materials should be addressed to K.A. (email: aoyama.kazuma@ist.osaka-u.ac.jp) or H.I. (email: iizuka@ist.osaka-u.ac.jp)

GVS RIDE: Providing a Novel Experience Using a Head Mounted Display and Four-pole Galvanic Vestibular Stimulation

Kazuma Aoyama
School of Interdisciplinary Mathematical Sciences, Meiji University
4-21-1 Nakano, Nakano-ku, Tokyo Japan
aoyama@meiji.ac.jp

Daiki Higuchi
Graduate School of Information Science and Technology, Osaka University
1-4 Yamadaoka, Suita, Osaka, 565-0871, Japan
Japan
daiki-higuchi@hiel.ist.osaka-u.ac.jp

Kenta Sakurai
Graduate School of Information Science and Technology, Osaka University
1-4 Yamadaoka, Suita, Osaka, 565-0871, Japan
Japan
kenta-sakurai@hiel.ist.osaka-u.ac.jp

Taro Maeda
Graduate School of Information Science and Technology, Osaka University
1-4 Yamadaoka, Suita, Osaka, 565-0871, Japan
t_maeda@ist.osaka-u.ac.jp

Hideyuki Ando
Graduate School of Information Science and Technology, Osaka University
1-4 Yamadaoka, Suita, Osaka, 565-0871, Japan
hide @ist.osaka-u.ac.jp

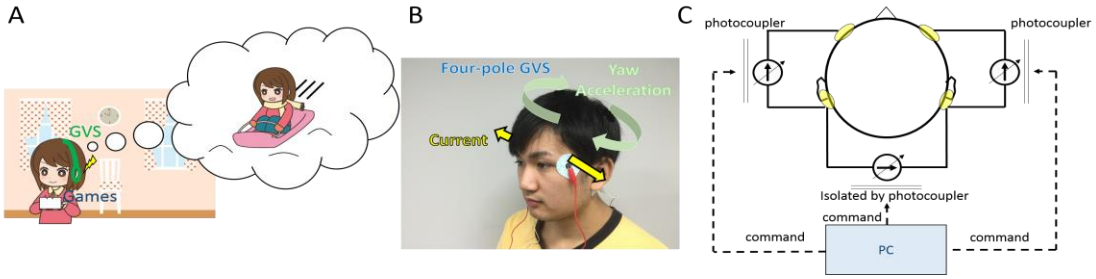

Figure 1: Use of Galvanic vestibular stimulus (GVS) for a virtual acceleration display and its composition.

ABSTRACT

Galvanic Vestibular Stimulation (GVS) is a technique that induces virtual acceleration (or virtual head motion) by the application of current to electrodes placed on the bilateral mastoids. Since the vestibular sensation closely resembles real-life sensation, it is a promising technique for virtual reality (VR) systems for presenting a highly realistic experience. However, the effect of conventional GVS is very weak. Moreover, GVS cannot induce lateral and anteroposterior directional acceleration. Thus, we invented methods to induce tri-directional acceleration (i.e., lateral, anteroposterior, and yaw rotation) to enhance virtual acceleration. The result is a new application named "GVS RIDE," which gives a highly realistic experience using four-pole GVS and a Head Mounted Display (HMD) in synchronization. This paper and our demo introduce our novel GVS method and an application using GVS with HMD.

SIGGRAPH '17 Emerging Technologies, July 30 - August 03, 2017, Los Angeles, CA, USA
ACM 978-1-4503-5012-9/17/07.
http://dx.doi.org/10.1145/3084822.3084840

CCS CONCEPTS

• **Human-centered computing → Interaction paradigms → Virtual reality**

KEYWORDS

galvanic vestibular stimulation, virtual head motion, multi direction, GVS RIDE.

Galvanic Vestibular Stimulation in Primates: Recording Vestibular Afferents during Transmastoid Stimulation

Annie Kwan

Department of Biomedical Engineering

McGill University

Montreal, Quebec, Canada

August 2016

A thesis submitted to McGill University in partial fulfillment

of the requirements of the degree of Master of Engineering

NEUROSCIENCE

Gating of social reward by oxytocin in the ventral tegmental area

Lin W. Hung,[1,2] Sophie Neuner,[1]* Jai S. Polepalli,[1]* Kevin T. Beier,[1,3,4]* Matthew Wright,[3,5] Jessica J. Walsh,[1] Eastman M. Lewis,[6] Liqun Luo,[3,4] Karl Deisseroth,[3,5] Gül Dölen,[6] Robert C. Malenka[1]†

The reward generated by social interactions is critical for promoting prosocial behaviors. Here we present evidence that oxytocin (OXT) release in the ventral tegmental area (VTA), a key node of the brain's reward circuitry, is necessary to elicit social reward. During social interactions, activity in paraventricular nucleus (PVN) OXT neurons increased. Direct activation of these neurons in the PVN or their terminals in the VTA enhanced prosocial behaviors. Conversely, inhibition of PVN OXT axon terminals in the VTA decreased social interactions. OXT increased excitatory drive onto reward-specific VTA dopamine (DA) neurons. These results demonstrate that OXT promotes prosocial behavior through direct effects on VTA DA neurons, thus providing mechanistic insight into how social interactions can generate rewarding experiences.

Positive prosocial experiences are critical for cooperative and productive interactions between members of a group. Conversely, the inability to experience reinforcement from social interactions (henceforth, "social reward") is a symptom of neuropsychiatric disorders, notably autism (*1*). Over the past decade, evidence has accumulated that the neuropeptide oxytocin (OXT) plays a critical role in social behaviors and may have therapeutic utility for the treatment of social behavior deficits (*2*). An important clue that OXT exerts some of its actions by influencing the brain's reward circuitry came from work demonstrating that OXT receptors (OXTrs) in the nucleus accumbens (NAc) of prairie voles were critical for pair bonding (*3*). Subsequent work suggested that OXT action in the NAc is also important for social reward in mice (*4*). OXT action in the ventral tegmental area (VTA), another key node of reward circuitry, may also be critical for regulating social interaction cues (*5*, *6*). Although social interactions in mice are accompanied by increases in activity in NAc-projecting VTA dopamine (DA) neurons (*7*), which are critical for motivated behaviors (*8*), the mechanism by which VTA DA neuron activity is gated during social behaviors is unknown.

Rabies virus–based tracing methods have suggested that OXT neurons in the paraventricular nucleus (PVN) send axonal projections to the VTA (*9*). To visualize these OXTergic projections directly, we injected AAV_{DJ}-DIO-eGFP (adeno-associated virus DJ with double-floxed inverse open reading frame flanking enhanced green fluorescent protein) into the PVN of a knock-in mouse line expressing Cre recombinase in OXT neurons (*OXTiresCre*) (Fig. 1A). Consistent with previous reports (*10*), we found colocalization of eGFP and OXT immunostaining in the PVN, with no detectable eGFP expression in vasopressin (AVP) PVN neurons (~48% of OXT neurons expressed eGFP in tissue sections from eight animals) (Fig. 1B). Axons expressing eGFP were present in the VTA (Fig. 1B), often in close proximity to OXTr-expressing DA neurons (Fig. 1C), which were localized using an OXTr-Venus knock-in mouse line (*11*). Tail-vein fluorogold injections revealed that both magnocellular and parvocellular PVN OXT neurons projected to the VTA (fig. S1).

To investigate whether PVN neurons projecting to the VTA are necessary for social reward, we inhibited these neurons by injecting a retrogradely transported canine adenovirus expressing Cre (CAV2-Cre) into the VTA and an AAV expressing a Cre-dependent inward rectifying potassium channel (AAV_{DJ}-DIO-Kir2.1-ZsGreen) into the PVN (Fig. 1D and fig. S2A). Two weeks after viral injections, mice were subjected to a social conditioned place preference (CPP) assay (*4*). Mice expressing the potassium channel (Kir2.1) in VTA-projecting PVN neurons exhibited reduced preference for the socially conditioned context (Fig. 1, F and G) compared with control mice expressing ZsGreen (Fig. 1, E and G). Expression of Kir2.1 in VTA-projecting PVN neurons did not influence the CPP generated by administration of cocaine (fig. S2, B to D) or locomotor activity (fig. S2E).

To test whether OXT action in the VTA is necessary for social reward, we selectively ablated OXTrs in the VTA by injecting an AAV_{DJ}-Cre-eGFP into the VTA of floxed OXTr ($OXTr^{fl/fl}$) mice (Fig. 1H) (*12*). Unlike wild-type mice injected with the same virus, mice lacking OXTrs in the VTA exhibited no social CPP (Fig. 1, I to K). To determine whether OXTrs specifically in DA neurons are necessary for social reward, we crossed $OXTr^{fl/fl}$ mice with *DATCre* mice (*13*) (Fig. 1L; fig. S3 illustrates the breeding strategy). Homozygous OXTr DA knockout (KO) mice exhibited no social CPP, whereas littermate control mice expressed normal social CPP, as did heterozygous OXTr DA KO mice (Fig. 1, M to O, and fig. S4, A to C). Deleting OXTrs from subpopulations of GABAergic cells by crossing $OXTr^{fl/fl}$ mice with *GAD2Cre* mice (Fig. 1P) had no effect on social CPP (Fig. 1, Q to S). All of these mouse lines exhibited CPP in response to cocaine and normal locomotor activity in the open field after saline and cocaine injections (fig. S4, D to K).

To determine whether activity in VTA-projecting PVN neurons increases during social interactions, we injected CAV2-Cre into the VTA of Ai14 tdTomato reporter mice to label cells projecting to the VTA (Fig. 2A) and assessed the expression of the immediate early gene *c-fos* (*14*). After social interaction, the proportion of VTA-projecting PVN neurons expressing *c-fos* tripled compared with that in mice that interacted with a toy mouse (Fig. 2B). To more directly measure PVN OXT neuronal activity during social interactions, we targeted the fluorescent calcium indicator GCaMP6m to PVN OXT neurons by injecting AAV_{DJ}-DIO-GCaMP6m into the PVN of *OXTiresCre* mice and performed fiber photometry (Fig. 2, C to E). No increase in fluorescent signal occurred when these mice interacted with a toy mouse (Fig. 2F). However, there was a time-locked increase in the activity of PVN OXT neurons during social contact with a juvenile (Fig. 2, G and H).

We next investigated whether optogenetic activation of PVN OXT neurons alone is rewarding by injecting a Cre-dependent AAV expressing ChETA (AAV_{DJ}-DIO-ChETA-eYFP) into the PVN of *OXTiresCre* mice and implanting optical fibers in the PVN (ChETA, channelrhodopsin-2 with threonine substituted for glutamic acid at position 123; eYFP, enhanced yellow fluorescent protein) (Fig. 2, I and J). *OXTiresCre* mice injected with AAV_{DJ}-DIO-eYFP served as controls. Consistent with previous results (*15*), optogenetic activation of PVN OXT neurons did not reinforce operant behaviors, as assayed using real-time CPP (RT-CPP) (Fig. 2K and fig. S5, A and B) and nose-poking for intracranial self-stimulation (ICSS) (Fig. 2L and fig. S5, C to G).

Because PVN OXT neuron activity appears to be important for social reward, yet their activation alone did not drive instrumental learning, we hypothesized that activation of these neurons in a social context would facilitate this type of learning. In a social RT-CPP (sRT-CPP) protocol, mice were exposed to a confined novel juvenile mouse on day 1 without any stimulation (Fig. 2M). On day 2, optogenetic stimulation occurred when mice entered the compartment containing the confined familiar

[1]Nancy Pritzker Laboratory, Department of Psychiatry and Behavioral Sciences, Stanford University, Stanford, CA, USA. [2]The Florey Institute of Neuroscience and Mental Health, Parkville, Victoria, Australia. [3]Howard Hughes Medical Institute, Stanford University, Stanford, CA, USA. [4]Department of Biology, Stanford University, Stanford, CA, USA. [5]Departments of Bioengineering and Psychiatry and Behavioral Sciences, Stanford University, Stanford, CA, USA. [6]Department of Neuroscience, John Hopkins University, Baltimore, MD, USA.
*These authors contributed equally to this work.
†Corresponding author. Email: malenka@stanford.edu

Cite as: J. J. Moore *et al.*, *Science* 10.1126/science.aaj1497 (2017).

Dynamics of cortical dendritic membrane potential and spikes in freely behaving rats

Jason J. Moore,[1,2]* Pascal M. Ravassard,[1,3] David Ho,[1,2] Lavanya Acharya,[1,4] Ashley L. Kees,[1,2] Cliff Vuong,[1,3] Mayank R. Mehta[1,2,3,5]*

[1]W. M. Keck Center for Neurophysics, Integrative Center for Learning and Memory, and Brain Research Institute, University of California at Los Angeles, Los Angeles, CA, USA. [2]Neuroscience Interdepartmental Program, University of California at Los Angeles, Los Angeles, CA, USA. [3]Department of Physics and Astronomy, University of California at Los Angeles, Los Angeles, CA, USA. [4]Biomedical Engineering Interdepartmental Program, University of California at Los Angeles, Los Angeles, CA, USA. [5]Departments of Neurology and Neurobiology, University of California at Los Angeles, Los Angeles, CA, USA.

*Corresponding author. Email: jason.moore@ucla.edu (J.J.M.); mayankmehta@ucla.edu (M.R.M.)

Neural activity in vivo is primarily measured using extracellular somatic spikes, which provide limited information about neural computation. Hence, it is necessary to record from neuronal dendrites, which generate dendritic action potentials (DAP) and profoundly influence neural computation and plasticity. We measured neocortical sub- and suprathreshold dendritic membrane potential (DMP) from putative distal-most dendrites using tetrodes in freely behaving rats over multiple days with a high degree of stability and sub-millisecond temporal resolution. DAP firing rates were several fold larger than somatic rates. DAP rates were modulated by subthreshold DMP fluctuations which were far larger than DAP amplitude, indicting hybrid, analog-digital coding in the dendrites. Parietal DAP and DMP exhibited egocentric spatial maps comparable to pyramidal neurons. These results have important implications for neural coding and plasticity.

Microelectrode techniques have enabled the long-term measurement of extracellular somatic action potentials in freely behaving subjects. However, somatic action potentials are brief (~1 ms), occur rarely (~1.5 Hz in principal neocortical neurons), and only represent the binary output of neurons, while the vast majority of excitatory synapses are localized on their dendritic arbors, each spanning more than 1000 μm (*1*). In vitro studies show that dendrites support local spike initiation of DAP (*2–16*) and back-propagating action potentials (bAP) initiated at cell somata (*5–8*, *12*, *13*, *15–22*). Measurements in anesthetized, head-fixed animals (*23–26*) support these findings. DAP affect synaptic integration (*16*, *27–33*) and endow neurons with greater computational power and information capacity (*14–16*, *29*, *30*, *32–38*) by turning dendritic branches into computational subunits with branch-specific plasticity (*9–11*, *14–16*, *30–32*).

Two-photon calcium imaging (*21*, *26*, *39*, *40*), sharp electrode (*2*), or patch-clamp techniques (*41*) can be used to study dendrites in vivo. However, calcium imaging is not a direct measure of subthreshold membrane potential or dendritic sodium spikes, and lacks sub-millisecond resolution. Sharp electrode and patch-clamp techniques damage or rupture the membrane, thus limiting the recording duration (*42*) and altering in vivo neural dynamics including firing rates (*43*); they are ill-suited to record from thin dendrites. Additionally, these methods often require the subject to be anesthetized or immobilized, which alter neural dynamics and limit possible behavioral paradigms.

Extracellular recording techniques can also, at times, record intracellular-like signals. Sharp glass pipettes occasionally measure "quasi-intracellular" somatic recordings in anesthetized animals (*44–48*). These recordings can be stable for at most a few hours (*45*), and the recorded spikes have identical shapes as somatic action potentials (~1 ms width) (*45*, *47*, *48*). Quasi-intracellular recordings are proposed to arise from a region of high electrical resistance electrically isolating the membrane under the microelectrode, resulting in large amplitude, intracellular-like signals. Microelectrode arrays can achieve an "in-cell" recording configuration (*49*, *50*) when cultured neurons engulf the recording electrodes, yielding a large seal resistance and allowing measurement of the intracellular voltage.

How might these phenomena be leveraged to investigate dendritic activity in vivo? We used chronically implanted tetrodes (*51*, *52*) (see Methods), which are often flexible and have a narrow profile to mitigate cell damage. Astrocytes and microglia can form a high impedance sheath around a tetrode and shield off the rest of the extracellular space (*53–55*). We hypothesized that this process can encapsulate a dendrite alongside the tetrode, such that the voltages at the tetrode tips approximate the intracellular (DMP), without penetrating the dendrite.

Results

We implanted 9 rats with hyperdrives containing up to 22

Adjustable refractive power from diffractive moiré elements

Stefan Bernet* and Monika Ritsch-Marte

Division for Biomedical Physics, Innsbruck Medical University, A-6020 Innsbruck, Austria

*Corresponding author: Stefan.Bernet@i-med.ac.at

Received 28 April 2008; revised 12 June 2008; accepted 13 June 2008;
posted 19 June 2008 (Doc. ID 95463); published 11 July 2008

We show how suitable combinations of cascaded diffractive optical elements (DOEs) can form a combined "moiré DOE" of adjustable refractive power and high diffraction efficiency. The optical power can be adjusted continuously by a mutual rotation of one DOE with respect to the other. Fresnel lenses and axicons of variable refractive power or spiral phase plates of adjustable helical charge can be realized this way. © 2008 Optical Society of America

OCIS codes: 050.1970, 120.4120, 220.4298.

1. Introduction

Diffractive optical elements (DOEs) are optical components consisting of microscopic phase structures in a transparent material [1]. Commercially available DOEs include lenses, arrays of lenses, or holograms (so-called kinoforms [2]) that project specified patterns, such as lines, crosshairs, or dot arrays. Each pixel of a DOE shifts the phase of an incident light beam within an interval between 0 and 2π. The transmitted wave then carries the predesigned wavefront modulation.

There exist many algorithms (e.g., kinoform algorithm, Gerchberg–Saxton algorithm [3], etc.) to calculate the DOEs dedicated to perform the desired tasks. In the production process of a DOE, the corresponding phase landscapes are imprinted into a material with techniques such as photolithography, electron beam lithography, or mechanical micromachining (diamond turning), such that each spot of the material delays the phase of an incoming light beam by the desired phase value. This can be achieved with either a modulated surface profile (which is, for example, etched into a quartz plate) or by a spatially modulated index of refraction as in, for example, a photopolymer film.

0003-6935/08/213722-09$15.00/0

An important difference of computer-generated DOEs, compared to normal holograms that are recorded by superposition of an object and a reference wave, is the fact that DOE phase structures are typically not harmonic; i.e., they locally correspond to blazed gratings with a sawtooth phase profile. As a result, the diffraction efficiency of a properly designed DOE can reach 100%, in contrast to the 40% achieved by normal phase holograms with harmonic grating structures.

The transmission function $T(x,y)$ of a DOE is a "phase-only landscape" of the form $T(x,y) = \exp[i\Phi(x,y)]$, where $\Phi(x,y)$ is an array of pixels in a range between 0 and 2π, corresponding to the phase shift a light beam acquires when passing through the corresponding spot. If two DOEs with transmission functions $T_1(x,y) = \exp[i\Phi_1(x,y)]$ and $T_2(x,y) = \exp[i\Phi_2(x,y)]$ are placed directly behind each other, then the transmission function T_{joint} of the combined DOE becomes

$$T_{\text{joint}}(x,y) = T_1(x,y)T_2(x,y) = \exp\{i[\Phi_1(x,y) + \Phi_2(x,y)]\}. \quad (1)$$

The principle of our suggested system is indicated in Fig. 1. Two DOEs are cascaded such that the resulting total transmission function can be changed continuously by a simple mutual rotation of the two DOEs. The underlying principle is similar to

NeuroResource

Neuron

Neural Circuit-Specialized Astrocytes: Transcriptomic, Proteomic, Morphological, and Functional Evidence

Highlights

- Multiple approaches were used to assess astrocyte diversity in two neural circuits
- Physiological and anatomical studies showed evidence for astrocyte functional diversity
- RNA-seq, proteomic, and cell marker analyses confirmed diversity
- Evidence is provided for brain neural-circuit-specialized astrocytes

Authors

Hua Chai, Blanca Diaz-Castro, Eiji Shigetomi, ..., Julian P. Whitelegge, Giovanni Coppola, Baljit S. Khakh

Correspondence

bkhakh@mednet.ucla.edu

In Brief

The Khakh lab used state-of-the-art optical, anatomical, electrophysiological, transcriptomic, and proteomic approaches to explore astrocyte similarities and differences in two neural circuits. Candid evaluation of the data across ten approaches provided not only strong evidence for astrocyte diversity but also an experimental workflow to explore astrocyte diversity across the brain.

Chai et al., 2017, Neuron *95*, 1–19
August 2, 2017
http://dx.doi.org/10.1016/j.neuron.2017.06.029

CellPress

Article

Neuron

Specialized Representations of Value in the Orbital and Ventrolateral Prefrontal Cortex: Desirability versus Availability of Outcomes

Highlights

- The VLPFC is necessary for updating stimulus-outcome probability estimates
- The OFC is necessary for updating stimulus-outcome values based on current needs
- The VLPFC is necessary for both contingent and noncontingent learning

Authors

Peter H. Rudebeck,
Richard C. Saunders,
Dawn A. Lundgren, Elisabeth A. Murray

Correspondence

peter.rudebeck@mssm.edu (P.H.R.),
murraye@mail.nih.gov (E.A.M.)

In Brief

Rudebeck et al. show that the orbitofrontal cortex (OFC) and ventrolateral prefrontal cortex (VLPFC) make dissociable contributions to decision-making. The VLPFC, but not the OFC, is critical for updating stimulus-outcome availability, whereas the OFC, but not the VLPFC, is vital for updating stimulus-outcome desirability.

Rudebeck et al., 2017, Neuron *95*, 1208–1220
August 30, 2017
http://dx.doi.org/10.1016/j.neuron.2017.07.042

CellPress

LETTER

doi:10.1038/nature19766

Autocrine BDNF–TrkB signalling within a single dendritic spine

Stephen C. Harward[1]*, Nathan G. Hedrick[1]*†, Charles E. Hall[1], Paula Parra-Bueno[2], Teresa A. Milner[3,4], Enhui Pan[1], Tal Laviv[2], Barbara L. Hempstead[3,5], Ryohei Yasuda[1,2] & James O. McNamara[1]

Brain-derived neurotrophic factor (BDNF) and its receptor TrkB are crucial for many forms of neuronal plasticity[1–6], including structural long-term potentiation (sLTP)[7,8], which is a correlate of an animal's learning[7,9–12]. However, it is unknown whether BDNF release and TrkB activation occur during sLTP, and if so, when and where. Here, using a fluorescence resonance energy transfer-based sensor for TrkB and two-photon fluorescence lifetime imaging microscopy[13–16], we monitor TrkB activity in single dendritic spines of CA1 pyramidal neurons in cultured murine hippocampal slices. In response to sLTP induction[9,14–16], we find fast (onset < 1 min) and sustained (>20 min) activation of TrkB in the stimulated spine that depends on NMDAR (*N*-methyl-D-aspartate receptor) and CaMKII signalling and on postsynaptically synthesized BDNF. We confirm the presence of postsynaptic BDNF using electron microscopy to localize endogenous BDNF to dendrites and spines of hippocampal CA1 pyramidal neurons. Consistent with these findings, we also show rapid, glutamate-uncaging-evoked, time-locked BDNF release from single dendritic spines using BDNF fused to superecliptic pHluorin[17–19]. We demonstrate that this postsynaptic BDNF–TrkB signalling pathway is necessary for both structural and functional LTP[20]. Together, these findings reveal a spine-autonomous, autocrine signalling mechanism involving NMDAR–CaMKII-dependent BDNF release from stimulated dendritic spines and subsequent TrkB activation on these same spines that is crucial for structural and functional plasticity.

To address the role of BDNF–TrkB signalling in sLTP, we developed a fluorescence resonance energy transfer (FRET)-based sensor for TrkB consisting of two components: (1) TrkB fused to monomeric enhanced green fluorescent protein (TrkB–eGFP), and (2) an SH2 domain of the TrkB binding partner phospholipase Cγ1 (PLC-γ1)[21] fused to two copies of monomeric red fluorescent protein-1 (mRFP1–PLC–mRFP1; Fig. 1a and Supplementary Information). After TrkB activation via phosphorylation of Tyr816, the affinity of mRFP1–PLC–mRFP1 for TrkB–eGFP increases[21], thereby allowing FRET to occur between the fluorophores (Supplementary Information). We validated the sensor in HeLa cells and cultured cortical neurons by showing it to be sensitive to BDNF, specific for Tyr816phosphorylation, and reversible when imaged by two-photon fluorescence lifetime imaging microscopy (2pFLIM) (Extended Data Fig. 1, Supplementary Information). Furthermore, we demonstrated that the sensor could functionally replace endogenous TrkB in neurons of cultured hippocampal slices (Extended Data Fig. 2, Supplementary Information).

Using this sensor, we biolistically transfected cultured rat hippocampal slices and imaged CA1 pyramidal neurons with 2pFLIM. In response to glutamate uncaging targeted to a single dendritic spine (30 pulses at 0.5 Hz), spine volume rapidly increased by ~220% (transient phase) before relaxing to an increased state of ~90% lasting at least 60 min (sustained phase; Fig. 1b, c, Extended Data Fig. 3a)—changes independent of protein synthesis (Extended Data Fig. 3c, d) and largely consistent with previous descriptions of sLTP (Extended Data Fig. 3a, Supplementary Information)[9,14–16]. At the same time, TrkB rapidly activated in the stimulated spine, peaking at ~1–2 min and remaining elevated for at least 60 min (Fig. 1b, d, e, Extended Data Figs 3b, 4 and Supplementary Information). For the first 30–60 s after the onset of glutamate uncaging, this activation was largely restricted to the stimulated spine (Fig. 1d–f, Supplementary Information). However, with time, TrkB activation in adjacent regions slowly increased, suggesting spreading of TrkB activation (Fig. 1d–f). The validity of the observed signal was confirmed by its dependence on kinase activity and Tyr816 phosphorylation and independence of sensor concentration and temperature (Extended Data Figs 5–7, Supplementary Information).

To explore mechanisms underlying this TrkB activation, we asked whether it required NMDAR-mediated Ca^{2+} influx[7,9,15,16] and subsequent CaMKII activation[9,15]. Application of either the NMDAR inhibitor D-2-amino-5-phosphonovalerate (D-AP5; 100 μM) or the CaMKII inhibitor CN21 (ref. 22; 10 μM) impaired TrkB activation during the transient and sustained phases of sLTP while also inhibiting spine volume change (Fig. 2a–d), suggesting that TrkB is in part downstream of both NMDAR and CaMKII activation.

Next, we asked whether BDNF contributes to this TrkB activation. Using the extracellular BDNF scavenger TrkB-Ig (6–8 μg ml^{-1}), we found impaired TrkB activation throughout sLTP with a similar impairment of spine volume change (Fig. 2e–h), suggesting a crucial role for BDNF in mediating glutamate-uncaging-induced TrkB activation. To examine the cellular source of BDNF underlying this activation, we sparsely transfected the sensor with Cre recombinase in slices from *Bdnf*$^{fl/fl}$ mice, thereby selectively knocking-out BDNF synthesized in the postsynaptic cell, a perturbation without detectable effect on basal spine morphology[23,40,41] (Extended Data Fig. 8a, b). This manipulation attenuated glutamate-uncaging-evoked TrkB activation and sLTP (Fig. 2i–l) while leaving CaMKII activation intact (Extended Data Fig. 8c–f). These results implicate autocrine BDNF as one mechanism underlying TrkB activation during sLTP: additional mechanisms could include other sources of BDNF (pre-synaptic, paracrine) or non-neurotrophin TrkB activators (such as zinc)[24].

The dependence of glutamate-uncaging-induced TrkB activation on postsynaptically synthesized BDNF controversially suggests the existence of BDNF in dendrites or spines[25]. To provide more direct evidence, we used electron microscopy to examine BDNF localization in a previously characterized mouse line in which a C-terminal haemagglutinin (HA) epitope tag was added to the *Bdnf* coding sequence (*Bdnf-HA*)[26]. Using highly sensitive antibodies against the HA-tag, we found BDNF not only in axons but also in dendrites and spines of CA1 pyramidal cells of these mice (Fig. 3).

[1]Neurobiology Department, Duke University Medical Center, Research Drive, Durham, North Carolina 27710, USA. [2]Max Planck Florida Institute for Neuroscience, 1 Max Planck Way, Florida 33458, USA. [3]Feil Family Brain and Mind Research Institute, Weill Cornell Medicine, 407 East 61st St, New York 10065, USA. [4]Laboratory of Neuroendocrinology, The Rockefeller University, 1230 York Avenue, New York 10065, USA. [5]Department of Medicine, Weill Cornell Medicine, 1300 York Avenue, New York 10065, USA. †Present address: Neurobiology Section, Center for Neural Circuits and Behavior, and Department of Neurosciences, University of California, San Diego, 9500 Gilman Drive, La Jolla, California 92093, USA.
*These authors contributed equally to this work.

frontiers in Neuroanatomy

REVIEW
published: 12 July 2017
doi: 10.3389/fnana.2017.00054

The Functioning of a Cortex without Layers

Julien Guy[1]* *and Jochen F. Staiger*[1,2]*

[1]*Institute for Neuroanatomy, University Medical Center Göttingen, Georg-August-University, Göttingen, Germany,*
[2]*DFG Center for Nanoscale Microscopy and Molecular Physiology of the Brain (CNMPB), Göttingen, Germany*

A major hallmark of cortical organization is the existence of a variable number of layers, i.e., sheets of neurons stacked on top of each other, in which neurons have certain commonalities. However, even for the neocortex, variable numbers of layers have been described and it is just a convention to distinguish six layers from each other. Whether cortical layers are a structural epiphenomenon caused by developmental dynamics or represent a functionally important modularization of cortical computation is still unknown. Here we present our insights from the reeler mutant mouse, a model for a developmental, "molecular lesion"-induced loss of cortical layering that could serve as ground truth of what an intact layering adds to the cortex in terms of functionality. We could demonstrate that the reeler neocortex shows no inversion of cortical layers but rather a severe disorganization that in the primary somatosensory cortex leads to the complete loss of layers. Nevertheless, the somatosensory system is well organized. When exploring an enriched environment with specific sets of whiskers, activity-dependent gene expression takes place in the corresponding modules. Precise whisker stimuli lead to the functional activation of somatotopically organized barrel columns as visualized by intrinsic signal optical imaging. Similar results were obtained in the reeler visual system. When analyzing pathways that could be responsible for preservation of tactile perception, lemniscal thalamic projections were found to be largely intact, despite the smearing of target neurons across the cortical mantle. However, with optogenetic experiments we found evidence for a mild dispersion of thalamic synapse targeting on layer IV-spiny stellate cells, together with a general weakening in thalamocortical input strength. This weakening of thalamic inputs was compensated by intracortical mechanisms involving increased recurrent excitation and/or reduced feedforward inhibition. In conclusion, a layer loss so far only led to the detection of subtle defects in sensory processing by reeler mice. This argues in favor of a view in which cortical layers are not an essential component for *basic* perception and cognition. A view also supported by recent studies in birds, which can have remarkable cognitive capacities despite the lack of a neocortex with multiple cortical layers. In conclusion, we suggest that future studies directed toward understanding cortical functions should rather focus on circuits specified by functional cell type composition than mere laminar location.

Keywords: neocortex, cortical circuits, reeler mutant mouse, developmental plasticity, optogenetics, lemniscal pathway

OPEN ACCESS

Edited by:
Kathleen S. Rockland, Boston University School of Medicine, United States

Reviewed by:
Andre Goffinet, Université catholique de Louvain, Belgium
Gabriella D'Arcangelo, Rutgers University, The State University of New Jersey, United States

***Correspondence:**
Julien Guy
julien.guy@med.uni-goettingen.de
Jochen F. Staiger
jochen.staiger@med.uni-goettingen.de

Received: *21 April 2017*
Accepted: *20 June 2017*
Published: *12 July 2017*

Citation:
Guy J and Staiger JF (2017) The Functioning of a Cortex without Layers. Front. Neuroanat. 11:54. doi: 10.3389/fnana.2017.00054

REPORT

MEMORY RESEARCH

Engrams and circuits crucial for systems consolidation of a memory

Takashi Kitamura,[1]* Sachie K. Ogawa,[1]* Dheeraj S. Roy,[1]* Teruhiro Okuyama,[1] Mark D. Morrissey,[1] Lillian M. Smith,[1] Roger L. Redondo,[1,2]† Susumu Tonegawa[1,2]‡

Episodic memories initially require rapid synaptic plasticity within the hippocampus for their formation and are gradually consolidated in neocortical networks for permanent storage. However, the engrams and circuits that support neocortical memory consolidation have thus far been unknown. We found that neocortical prefrontal memory engram cells, which are critical for remote contextual fear memory, were rapidly generated during initial learning through inputs from both the hippocampal–entorhinal cortex network and the basolateral amygdala. After their generation, the prefrontal engram cells, with support from hippocampal memory engram cells, became functionally mature with time. Whereas hippocampal engram cells gradually became silent with time, engram cells in the basolateral amygdala, which were necessary for fear memory, were maintained. Our data provide new insights into the functional reorganization of engrams and circuits underlying systems consolidation of memory.

Memories are thought to be initially stored within the hippocampal–entorhinal cortex (HPC-EC) network (recent memory) and, over time, slowly consolidated within the neocortex for permanent storage (remote memory) (*1*–*7*). Systems memory consolidation models suggest that the interaction between the HPC-EC network and the neocortex during and after an experience is crucial (*8*–*12*). Experimentally, prolonged inhibition of hippocampal or neocortical networks during the consolidation period produces deficits in remote memory formation (*13*–*15*). However, little is known regarding specific neural circuit mechanisms underlying the formation and maturation of neocortical memories through interactions with the HPC-EC network. Using activity-dependent cell-labeling technology (*16*–*18*), combined with viral vector–based transgenic, anatomical (*19*, *20*), and optogenetic strategies (*19*, *21*) for circuit-specific manipulations and in vivo calcium imaging (*22*), we investigated the nature and dynamics of neocortical and subcortical memory engram cells [a population of neurons that are activated by learning, have enduring cellular changes, and are reactivated by a part of the original stimuli for recall (*18*)] and their circuits for systems consolidation of memory.

We first traced entorhinal projections to frontal cortical structures [the medial prefrontal cortex (PFC), caudal anterior cingulate cortex (cACC), and retrosplenial cortex (RSC)] involved in contextual fear memory, as well as to the basolateral amygdala (BLA), with injections of the retrograde tracer cholera toxin subunit B–Alexa*555* (hereafter, CTB injections) into these regions (fig. S1). CTB injections resulted in labeling in the medial entorhinal cortex (MEC), specifically in cells in layer Va (Fig. 1, A to D and H, and fig. S2, A to D), indicating that MEC-Va cells have extensive projections to the neocortex and BLA (*23*). We then sought to inhibit these specific projections by bilaterally injecting adeno-associated virus 8 (AAV_8)–calcium/calmodulin-dependent protein kinase II (CaMKII):eArchT–enhanced yellow fluorescent protein (eYFP) in the deep layers of the MEC in wild-type (WT) mice with bilaterally implanted optic fibers above the PFC, cACC, or RSC (Fig. 1, E and J, and fig. S2G). Expression of eArchT-eYFP was abundant in MEC-Va terminals located in each of these regions (Fig. 1, B and I, and fig. S2D). These mice were then subjected to contextual fear conditioning (CFC) while we delivered green light bilaterally to the different cortical areas that have MEC-Va projections during either the conditioning period (day 1) (fig. S2E) or the recall test period (days 2, 8, 15, and 22) (fig. S2F). Axon terminal inhibition with optogenetics of MEC-Va cells within the PFC during day 1 of CFC disrupted memory at days 15 and 22, but not at days 2 or 8 (Fig. 1F). Terminal inhibition during memory recall tests did not affect memory retrieval (Fig. 1G). Last, terminal inhibition in the cACC or RSC during CFC or recall had no effect on memory throughout these periods (Fig. 1, J to L, and fig. S2, G to I).

The above results suggest that MEC-Va input into the PFC during CFC is crucial for the eventual formation of remote memory. This hypothesis was supported by several findings. First, CFC increased the number of c-Fos^+ cells in the PFC compared with that in the PFC of home-cage mice (Fig. 1, M to O), whereas context-only exposure did not increase c-Fos activity in the PFC (Fig. 1O). Second, optogenetic terminal inhibition of MEC-Va projections within the PFC during CFC inhibited the observed increase of c-Fos^+ cells in the PFC (Fig. 1O). Last, we identified CFC engram cells in the PFC. We targeted injections of AAV_9–c-fos:tetracycline-controlled transactivator (tTA) and AAV_9–tetracycline response element (TRE):channelrhodopsin-2 (ChR2)–mCherry (Fig. 1, P and Q) and optic fibers to the PFC of WT mice and labeled the PFC cells activated by CFC with ChR2 while the mice were off doxycycline (Fig. 1R). Blue light stimulation at 4 Hz, but not at the conventional 20 Hz, of ChR2-mCherry–expressing cells in the PFC induced increased freezing behavior on days 2 and 12 in an unconditioned context (Fig. 1S and fig. S3), compared with freezing under the blue light–off condition. This blue light–induced freezing was prevented when MEC-Va fibers in the PFC were inhibited during CFC on day 1 (Fig. 1, T and U, and fig. S4). Using transsynaptic retrograde tracing combined with the activity-dependent cell labeling, we confirmed that the PFC engram cells generated by CFC received monosynaptic input from MEC-Va cells (Fig. 1, V to X, and fig. S5).

To examine whether PFC engram cells are also reactivated by the conditioned context (rather than by blue light) at recent and remote time points, we targeted injections of AAV_9-TRE:human histone H2B–green fluorescent protein (H2B-GFP) to the PFC of c-fos:tTA transgenic mice (Fig. 2A). The mice underwent CFC on day 1 and then were reexposed to the conditioned (context A) or an unconditioned (context B) context on days 2 or 13 (Fig. 2B). Cells activated by CFC were labeled with H2B-GFP, and the cells activated by the context test were labeled with a c-Fos antibody; we calculated the proportion of double-labeled cells (Fig. 2, A to B, and fig. S6B). Compared with H2B-GFP^- cells, H2B-GFP^+ cells (PFC engram cells) were preferentially reactivated in context A on day 13, but not on day 2 (Fig. 2C). There was no difference in c-Fos expression between H2B-GFP^+ and H2B-GFP^- cells when mice were tested in context B (Fig. 2C). We also found that the spine density of the PFC engram cells on day 12 was significantly higher than on day 2 (Fig. 2, D and E, and fig. S7), in line with previous findings of a positive correlation between the dendritic spine density of memory engram cells and memory expression triggered by natural recall cues (*24*–*26*).

To test whether PFC engram cells are necessary for memory recall by natural cues, we bilaterally targeted injections of AAV_9–c-fos:tTA and AAV_9-TRE:ArchT-eGFP (Fig. 2, D and F) and optic fibers to the PFC of WT mice and labeled the PFC engram cells that were activated by CFC with ArchT while the mice were off doxycycline (Fig. 2F). Cell body inhibition of the

[1]RIKEN-MIT Center for Neural Circuit Genetics at the Picower Institute for Learning and Memory, Departments of Biology and Brain and Cognitive Sciences, Massachusetts Institute of Technology, Cambridge, MA 02139, USA. [2]Howard Hughes Medical Institute, Massachusetts Institute of Technology, Cambridge, MA 02139, USA.
*These authors contributed equally to this work. †Present address: Roche Pharmaceutical Research and Early Development, Roche Innovation Center, F. Hoffmann-La Roche, Basel, Switzerland.
‡Corresponding author. Email: tonegawa@mit.edu

Please cite this article in press as: Parvizi et al., The Will to Persevere Induced by Electrical Stimulation of the Human Cingulate Gyrus, Neuron (2013), http://dx.doi.org/10.1016/j.neuron.2013.10.057

Neuron
Case Study

The Will to Persevere Induced by Electrical Stimulation of the Human Cingulate Gyrus

Josef Parvizi,[1,*] Vinitha Rangarajan,[1] William R. Shirer,[2] Nikita Desai,[1] and Michael D. Greicius[2]
[1]Laboratory of Behavioral and Cognitive Neurology (LBCN), Stanford Human Intracranial Cognitive Electrophysiology Program (SHICEP)
[2]Functional Imaging in Neuropsychiatric Disorders (FIND) Lab
Department of Neurology & Neurological Sciences, Stanford University, Stanford, CA 94305, USA
*Correspondence: jparvizi@stanford.edu
http://dx.doi.org/10.1016/j.neuron.2013.10.057

SUMMARY

Anterior cingulate cortex (ACC) is known to be involved in functions such as emotion, pain, and cognitive control. While studies in humans and nonhuman mammals have advanced our understanding of ACC function, the subjective correlates of ACC activity have remained largely unexplored. In the current study, we show that electrical charge delivery in the anterior midcingulate cortex (aMCC) elicits autonomic changes and the expectation of an imminent challenge coupled with a determined attitude to overcome it. Seed-based, resting-state connectivity analysis revealed that the site of stimulation in both patients was at the core of a large-scale distributed network linking aMCC to the frontoinsular and frontopolar as well as some subcortical regions. This report provides compelling, first-person accounts of electrical stimulation of this brain network and suggests its possible involvement in psychopathological conditions that are characterized by a reduced capacity to endure psychological or physical distress.

INTRODUCTION

The greatest of life's challenges leave us mired in "a sea of troubles," battered by the "slings and arrows of outrageous fortune" (Shakespeare, 1603). It is at such moments that an individual's will to persevere is put to the test. While some are able to marshal the necessary physical and psychological resources in the face of challenges, others have a pathologically lowered motivation and mental strength for enduring physical or psychological pain. Understanding the structure and physiology of the brain networks mediating attributes, such as the resolve to overcome upcoming challenges, will create new diagnostic and therapeutic frontiers for disorders such as depression and chronic pain that are characterized, in part, by reduced motivation, endurance, and perseverance.

Two lines of evidence suggest that the anterior cingulate cortex (ACC) and a set of connected regions might be the key network in this context. First, studies in humans and nonhuman mammals suggest that the ACC (including its midcingulate region) is essential for initiating changes in behavior, making associations between reward and action, determining the action necessary to obtain a goal, and synthesizing information about reinforcers ranging from pain and threatening conspecifics to aversive cues and negative feedback (Carter et al., 1999; Devinsky et al., 1995; Hayden et al., 2009; Rushworth et al., 2011; Shackman et al., 2011; Shenhav et al., 2013; Vogt and Sikes, 2000). Second, the ACC is anatomically well situated for such functions. For instance, anatomical tracing studies in nonhuman primates, as well as tractography and functional connectivity studies in humans, have suggested strong anatomical and functional connectivity between the ACC and brain structures known to be important for pain, pleasure, emotion, and decision making (for original references see Seeley et al., 2007; Van Hoesen et al., 1996; Vogt et al., 2004).

While lesion studies in humans have shown that the ACC is important for decision making and emotional processing, the anatomical imprecision of this approach can be problematic. It is often unclear the extent to which the cognitive and behavioral deficits in these patients are due to the compromise of the ACC itself rather than the adjacent cortical gray and white matter tissue frequently included in the lesion. In addition, subjective correlates of ACC activity have been methodologically difficult to assess given its hidden position deep within the mesial surface of the brain.

In the current multimodal study, we provide detailed, first-person accounts of neuromodulation in the anterior midcingulate cortex (aMCC) and its associated functional network using a combination of electrical brain stimulation (EBS) and preoperative resting-state functional magnetic resonance imaging (fMRI) in two epilepsy patients implanted with intracranial electrodes. In both patients, we demonstrate a remarkably stereotyped set of autonomic, cognitive, and emotional changes and establish a common functional connectivity map linking the aMCC stimulation site to a distributed network of regions, often referred to as the "emotional salience" or "cingulo-opercular" network (Seeley et al., 2007).

RESULTS

Two patients with refractory epilepsy were implanted with intracranial depth electrodes to localize the source of seizure activity. We localized the anatomical position of intracranial electrodes in each subject's native neuroanatomical space. As part of their routine clinical diagnosis, a volley of electrical charge was

Abel Lajtha
Editor
Guido Tettamanti
Gianfrancesco Goracci
Volume Editors

SPRINGER
REFERENCE

Handbook of Neurochemistry and Molecular Neurobiology

3rd Edition

Neural Lipids

Springer

On cell surface deformation during an action potential

Christian Fillafer[a], Matan Mussel[a,b], Julia Muchowski[a], Matthias F. Schneider[a]

[a]Technical University of Dortmund
Department of Physics
44227 Dortmund
Germany

[b]University of Augsburg
Department of Physics
86159 Augsburg
Germany

[1]**Address correspondence to:** Dr. Matthias Schneider
Technische Universität Dortmund
Medizinische und Biologische Physik
Otto-Hahn-Str. 4
44227 Dortmund
tel: +49-231-755-4139
email: matthias-f.schneider@tu-dortmund.de

Keywords: action potential; *Chara*; mechanical; membrane; cell surface

REVIEW SUMMARY

NEURODEVELOPMENT

Intersection of diverse neuronal genomes and neuropsychiatric disease: The Brain Somatic Mosaicism Network

Michael J. McConnell,*† John V. Moran,*† Alexej Abyzov, Schahram Akbarian, Taejeong Bae, Isidro Cortes-Ciriano, Jennifer A. Erwin, Liana Fasching, Diane A. Flasch, Donald Freed, Javier Ganz, Andrew E. Jaffe, Kenneth Y. Kwan, Minseok Kwon, Michael A. Lodato, Ryan E. Mills, Apua C. M. Paquola, Rachel E. Rodin, Chaggai Rosenbluh, Nenad Sestan, Maxwell A. Sherman, Joo Heon Shin, Saera Song, Richard E. Straub, Jeremy Thorpe, Daniel R. Weinberger, Alexander E. Urban, Bo Zhou, Fred H. Gage, Thomas Lehner, Geetha Senthil, Christopher A. Walsh, Andrew Chess, Eric Courchesne, Joseph G. Gleeson, Jeffrey M. Kidd, Peter J. Park, Jonathan Pevsner, Flora M. Vaccarino, Brain Somatic Mosaicism Network‡

BACKGROUND: Elucidating the genetic architecture of neuropsychiatric disorders remains a major scientific and medical challenge. Emerging genomic technologies now permit the analysis of somatic mosaicism in human tissues. The measured frequencies of single-nucleotide variants (SNVs), small insertion/deletion (indel) mutations, structural variants [including copy number variants (CNVs), inversions, translocations, and whole-chromosome gains or losses], and mobile genetic element insertions (MEIs) indicate that each neuron may harbor hundreds of somatic mutations. Given the long life span of neurons and their central role in neural circuits and behavior, somatic mosaicism represents a potential mechanism that may contribute to neuronal diversity and the etiology of numerous neuropsychiatric disorders.

ADVANCES: Somatic mutations that confer cellular proliferative or cellular survival phenotypes have been identified in patients with cortical malformations. These data have led to the hypothesis that somatic mutations may also confer phenotypes to subsets of neurons, which could increase the risk of developing certain neuropsychiatric disorders. Genomic technologies, including advances in long-read, next-generation DNA sequencing technologies, single-cell genomics, and cutting-edge bioinformatics, can now make it possible to determine the types and frequencies of somatic mutations within the human brain. However, a comprehensive understanding of the contribution of somatic mosaicism to neurotypical brain development and neuropsychiatric disease requires a coordinated, multi-institutional effort.

The National Institute of Mental Health (NIMH) has formed a network of 18 investigative teams representing 15 institutions called the Brain Somatic Mosaicism Network (BSMN). Each research team will use an array of genomic technologies to exploit well-curated human tissue repositories in an effort to define the frequency and pattern of somatic mutations in neurotypical individuals and in schizophrenia, autism spectrum disorder, bipolar disorder, Tourette syndrome, and epilepsy patient populations. Collectively, these efforts are estimated to generate a community resource of more than 10,000 DNA-sequencing data sets and will enable a cross-platform integrated analysis with other NIMH initiatives, such as the PsychENCODE project and the CommonMind Consortium.

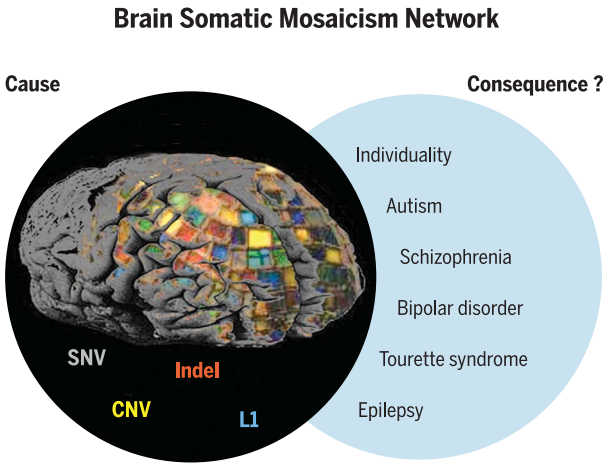

Collectively, somatic SNVs, indels, structural variants (e.g., CNVs), and MEIs (e.g., L1 retrotransposition events) shape the genomic landscape of individual neurons. The Brain Somatic Mosaicism Network aims to systematically generate pioneering data on the types and frequencies of brain somatic mutations in both neurotypical individuals and those with neuropsychiatric disease. The resulting data will be shared as a large community resource.

OUTLOOK: A fundamental open question in neurodevelopmental genetics is whether and how somatic mosaicism may contribute to neuronal diversity within the neurotypical spectrum and in diseased brains. Healthy individuals may harbor known pathogenic somatic mutations at subclinical frequencies, and the local composition of neural cell types may be altered by mutations conferring prosurvival phenotypes in subsets of neurons. By extension, the neurotypical architecture of somatic mutations may confer circuit-level differences that would not be present if every neuron had an identical genome. Given the apparent abundance of somatic mutations within neurons, an in-depth understanding of how different types of somatic mosaicism affect neural function could yield mechanistic insight into the etiology of neurodevelopmental and neuropsychiatric disorders.

ON OUR WEBSITE

Read the full article at http://dx.doi.org/10.1126/science.aal1641

The BSMN will examine large collections of postmortem brain tissue from neurotypical individuals and patients with neuropsychiatric disorders. By sequencing brain DNA and single neuronal genomes directly, rather than genomic DNA derived from peripheral blood or other somatic tissues, the BSMN will test the hypothesis that brain somatic variants contribute to neuropsychiatric disease. Notably, it is also possible that some inherited germline variants confer susceptibility to disease, which is later exacerbated by somatic mutations. Confirming such a scenario could increase our understanding of the genetic risk architecture of neuropsychiatric disease and may, in part, explain discordant neuropsychiatric phenotypes between identical twins. Results from these studies may lead to the discovery of biomarkers and genetic targets to improve the treatment of neuropsychiatric disease and may offer hope for improving the lives of patients and their families. ■

Author affiliations are available in the full article online.
*These authors contributed equally to this work.
†Corresponding author. Email: mikemc@virginia.edu (M.J.M.); moranj@umich.edu (J.V.M.)
‡Full membership of the Brain Somatic Mosaicism Network is listed in the supplementary materials.
Cite this article as M. J. McConnell *et al.*, *Science* **356**, eaal1641 (2017). DOI: 10.1126/science.aal1641

Article

Cell

Distinct Neural Circuits for the Formation and Retrieval of Episodic Memories

Graphical Abstract

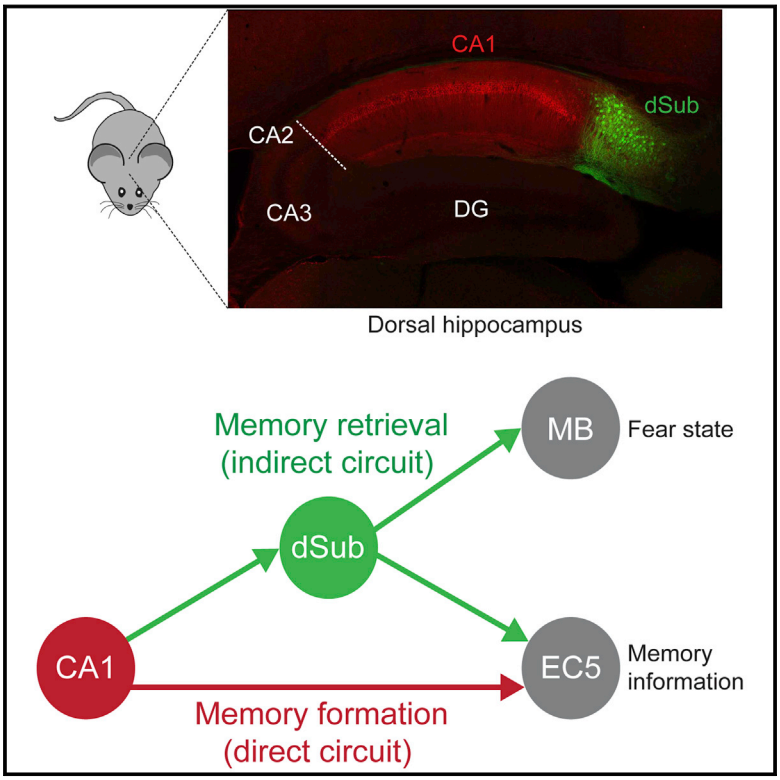

Authors

Dheeraj S. Roy, Takashi Kitamura, Teruhiro Okuyama, ..., Yuichi Obata, Atsushi Yoshiki, Susumu Tonegawa

Correspondence

tonegawa@mit.edu

In Brief

Episodic memories are formed and retrieved through distinct hippocampal pathways.

Highlights

- dSub and the circuit, CA1 → dSub → EC5, are required for hippocampal memory retrieval
- The direct CA1 → EC5 circuit is essential for hippocampal memory formation
- The dSub → MB circuit regulates memory-retrieval-induced stress hormone responses
- The dSub → EC5 circuit contributes to context-dependent memory updating

Roy et al., 2017, Cell *170*, 1–13
August 24, 2017
http://dx.doi.org/10.1016/j.cell.2017.07.013

CellPress

Cite as: Y. Zhai *et al.*, *Science* 10.1126/science.aai7899 (2017).

Scalable-manufactured randomized glass-polymer hybrid metamaterial for daytime radiative cooling

Yao Zhai,[1]* Yaoguang Ma,[1]* Sabrina N. David,[2] Dongliang Zhao,[1] Runnan Lou,[3] Gang Tan,[4] Ronggui Yang,[1]† Xiaobo Yin[1,2]†

[1]Department of Mechanical Engineering, University of Colorado, Boulder, CO 80309, USA. [2]Materials Science and Engineering Program, University of Colorado, Boulder, CO 80309, USA. [3]Department of Aerospace Engineering Sciences, University of Colorado, Boulder, CO 80309, USA. [4]Department of Civil and Architectural Engineering, University of Wyoming, Laramie, WY 82071, USA.

*These authors contributed equally to this work.

†Corresponding author. Email: xiaobo.yin@colorado.edu (X.Y); ronggui.yang@colorado.edu (R.Y.)

Passive radiative cooling draws heat from surfaces and radiates it into space as infrared radiation to which the atmosphere is transparent. However, the energy density mismatch between solar irradiance and the low infrared radiation flux from a near-ambient-temperature surface require materials that strongly emit thermal energy and barely absorb sunlight. We embedded resonant polar dielectric microspheres randomly in a polymeric matrix, resulting in a metamaterial that is fully transparent to the solar spectrum while having an infrared emissivity greater than 0.93 across the atmospheric window. When backed with silver coating, the metamaterial shows a noon-time radiative cooling power of 93 W/m^2 under direct sunshine. More critically, we demonstrated high-throughput, economical roll-to-roll manufacturing of the metamaterial, vital for promoting radiative cooling as a viable energy technology.

Radiative cooling—deposition of blackbody radiation from a hot object through the infrared transparency window of the atmosphere to the cold sink of outer space—is an appealing concept for the 21st century, where most daily necessities, from power generation to data centers, generate excess heat. In contrast to most of the currently employed cooling methods which require energy and resources to carry heat away, radiative cooling is a passive enhancement of the earth's natural method of cooling itself. Efficient nighttime radiative cooling systems have been extensively investigated in the past, with promising infrared-emissivity in both organic and inorganic materials including pigmented paints (*1*–*5*). Daytime radiative cooling, however, presents a different challenge because solar absorbance of just a few percent exceeds the cooling power and effectively heat the surface. Recently proposed nanophotonic devices can effectively reject solar irradiance but emit strongly in infrared (*6*, *7*), promising for daytime radiative cooling. However, the nanophotonic approach requires stringent, nanometer-precision fabrication, which is difficult to scale up cost-effectively to meet the large area requirements of the residential and commercial applications that can benefit most from radiative cooling.

Polymeric photonics is a growing field attractive for economy and scalability (*8*–*11*). Hybridization of random optical metamaterials with polymer photonics can be a promising approach for efficient daytime radiative cooling—To date harnessing randomness in photonic systems has yielded amplified spontaneous emission (*12*, *13*), extremely localized electromagnetic hotspots (*14*–*16*), improved light-trapping efficiency of photovoltaic cells (*17*, *18*), and negative permeability and switching devices with multi-stability (*19*, *20*). When electromagnetic resonators in a random metamaterial are collectively excited, the extinction and the optical path length in the material are both enhanced, resulting in nearly perfect absorption at the resonance (*21*, *22*). This implies the great potential for utilizing metamaterials with randomly distributed optical resonators for effective radiative cooling if perfect absorption (emissivity) across the entire atmospheric transmission window can be achieved.

Here, we demonstrate efficient day- and nighttime radiative cooling with a randomized, glass-polymer hybrid metamaterial. The metamaterial consists of a visibly transparent polymer encapsulating randomly distributed silicon dioxide (SiO_2) microspheres. The spectroscopic response spans two orders of magnitude in wavelength (0.3 to 25 μm). Our hybrid metamaterial is extremely emissive across the entire atmospheric transmission window (8-13 μm) due to phonon-enhanced Fröhlich resonances of the microspheres. A 50-μm-thick metamaterial film containing 6% of microspheres by volume has an averaged infrared emissivity > 0.93 and reflects approximately 96% of solar irradiance when backed with a 200-nm-thick silver coating. We experimentally demonstrate an average noon-time (11am – 2pm) radiative cooling power of 93 W/m^2 under direct sunshine during a three-day field test, and an average cooling power > 110 W/m^2 over the continuous 72-hour day and

Hippocampal Spike-Timing Correlations Lead to Hexagonal Grid Fields

Mauro M. Monsalve-Mercado and Christian Leibold
Department Biologie II & Graduate School of Systemic Neurosciences, LMU Munich, Großhadernerstr. 2, 82152 Planegg, Germany, and Bernstein Center for Computational Neuroscience Munich, Großhadernerstr. 2, 82152 Planegg, Germany

(Received 10 February 2017; revised manuscript received 16 May 2017; published 19 July 2017)

Space is represented in the mammalian brain by the activity of hippocampal place cells, as well as in their spike-timing correlations. Here, we propose a theory for how this temporal code is transformed to spatial firing rate patterns via spike-timing-dependent synaptic plasticity. The resulting dynamics of synaptic weights resembles well-known pattern formation models in which a lateral inhibition mechanism gives rise to a Turing instability. We identify parameter regimes in which hexagonal firing patterns develop as they have been found in medial entorhinal cortex.

DOI: 10.1103/PhysRevLett.119.038101

The spatial position of an animal can be reliably decoded from the neuronal activity of several cell populations in the hippocampal formation [1–3]. For example, place cells in the hippocampus fire at only a few locations in a spatial environment [4,5], and the position of the animal can be readily read out from single active neurons. Grid cells of the medial entorhinal cortex (MEC) fire at multiple distinct places that are arranged on a hexagonal lattice [6,7]. Although hexagonal patterns are abundant in nature and there exist well-studied physical theories for their emergence, the mechanistic origin of this neuronal grid pattern is still unclear. Initially, it was suggested that they result from continuous attractor dynamics [8,9] or the superposition of plane wave inputs [10] and, based on circuit anatomy, place cells would then result from a superposition of many grid cells [11,12]. More recent experiments, however, reported place cell activity without intact grid cells such that grid cells are not the unique determinants of place field firing [13–17]. Conversely, it would thus be possible that grid fields may arise from place field input as suggested in [18–20]. The biological mechanisms proposed by these latter theories, however, remain hypothetical. In the present Letter, we propose a learning rule for grid cells, based on the individual spike timings of place cells using spike-timing-dependent synaptic plasticity (STDP) [21–23]. The theory thereby predicts that the observed temporal hippocampal firing patterns (phase precession and theta-scale correlations, see below) [24–26] translate the temporal proximity of sequential place field spikes into spatial neighborhood relations, observed in grid-field activity. For our model to work, we only have to assume that the synaptic plasticity rule averages over a sufficiently long time interval.

Model.—We use the classical formulation of pairwise additive STDP [22,27], where the update of a synaptic weight J_n, $n = 1, \ldots, N$ at time t is computed as [22]

$$\frac{d}{dt}J_n = \int_{-\infty}^{\infty} ds W(s) C_n(s) + F(J_n). \tag{1}$$

$C_n(s)$ denotes the time-averaged correlation function between the spike train of the presynaptic neuron n and the postsynaptic neuron, the learning window $W(s)$ describes the update of the synaptic weight as a function of the time difference s between a pair of pre- and postsynaptic action potentials, and the function F implements soft bounds for the weight increase. The dynamics is further constrained such that weights cannot become negative.

To be able to treat Eq. (1) analytically, we use a linear Poisson neuron model; i.e., the mean firing rate of the postsynaptic neuron $E(t) = \mathbf{J} \cdot \mathbf{H}(t)$ results from a weighted sum of hippocampal firing rates $\mathbf{H} = (H_1(t), \ldots, H_N(t))^T$. Under these assumptions, $C_n(s)$ can be approximated for large N [22] as $C_n(s) = \sum_{n'} J_{n'} C_{nn'}(s)$, with

$$C_{nn'}(s) := \int_{-\infty}^{\infty} dt H_n(t) H_{n'}(t - s). \tag{2}$$

Inserting the correlation functions from Eq. (2) into the weight dynamics from Eq. (1) yields

$$\frac{d}{dt}J_n = \sum_{n'} J_{n'} G_{nn'} + F(J_n), \quad G_{nn'} := \int_{-\infty}^{\infty} ds W(s) C_{nn'}(s). \tag{3}$$

Following [28,29], we introduce the quadratic stabilization term $F(J) = F_0 J(K - J)$, $F_0 > 0$ that implements a soft upper bound.

As an input to the postsynaptic neuron, we consider a population of N hippocampal place cells. The firing of these neurons is characterized by a bell-shaped envelope, modulating the spatial path $x_{\mathcal{P}}(t)$ and oscillations in time t [Fig. 1(a)]

$$H_n(t; \mathcal{P}) = a e^{\frac{-[x_{\mathcal{P}}(t) - x_n]^2}{2\sigma^2}} [\cos(\omega t + \phi_n) + 1]/2. \tag{4}$$

The oscillation frequency ω of a neuron is slightly higher than the frequency $\omega_\theta/(2\pi)$ of the theta oscillation (~8 Hz)

LETTER

doi:10.1038/nature19784

Rho GTPase complementation underlies BDNF-dependent homo- and heterosynaptic plasticity

Nathan G. Hedrick[1]*†, Stephen C. Harward[1]*, Charles E. Hall[1], Hideji Murakoshi[2], James O. McNamara[1] & Ryohei Yasuda[1,3]

The Rho GTPase proteins Rac1, RhoA and Cdc42 have a central role in regulating the actin cytoskeleton in dendritic spines[1], thereby exerting control over the structural and functional plasticity of spines[2–5] and, ultimately, learning and memory[6–8]. Although previous work has shown that precise spatiotemporal coordination of these GTPases is crucial for some forms of cell morphogenesis[9], the nature of such coordination during structural spine plasticity is unclear. Here we describe a three-molecule model of structural long-term potentiation (sLTP) of murine dendritic spines, implicating the localized, coincident activation of Rac1, RhoA and Cdc42 as a causal signal of sLTP. This model posits that complete tripartite signal overlap in spines confers sLTP, but that partial overlap primes spines for structural plasticity. By monitoring the spatiotemporal activation patterns of these GTPases during sLTP, we find that such spatiotemporal signal complementation simultaneously explains three integral features of plasticity: the facilitation of plasticity by brain-derived neurotrophic factor (BDNF), the postsynaptic source of which activates Cdc42 and Rac1, but not RhoA; heterosynaptic facilitation of sLTP, which is conveyed by diffusive Rac1 and RhoA activity; and input specificity, which is afforded by spine-restricted Cdc42 activity. Thus, we present a form of biochemical computation in dendrites involving the controlled complementation of three molecules that simultaneously ensures signal specificity and primes the system for plasticity.

Previous studies using two-photon fluorescence lifetime imaging (2pFLIM) in combination with fluorescence resonance energy transfer (FRET)-based biosensors revealed that the Rho GTPases Cdc42 and RhoA had distinct spatial profiles during sLTP, with Cdc42 showing synapse-restricted activity and RhoA showing a diffuse, heterosynaptic pattern[3]. To obtain a more complete understanding of the spatiotemporal patterning of Rho GTPase activity during sLTP, we developed a FRET-based sensor for Rac1, following the design of the Cdc42 and RhoA sensors[3] (Fig. 1a; validation in Extended Data Figs 1–3). We transfected rat organotypic hippocampal slices with the sensor using biolistics[10,11] and imaged CA1 pyramidal neurons using 2pFLIM[12]. When sLTP was induced in single dendritic spines with two-photon glutamate uncaging[13,14] (Fig. 1b, c), Rac1 was rapidly (within ~1 min) activated in the stimulated spine, and remained active for at least 30 min (Fig. 1b, d), notably displaying a more pronounced sustained phase than RhoA or Cdc42 (ref. 3). This activation initially showed limited diffusion, after which it slowly spread over ~10 μm of the parent dendrite until it nearly equalized with activity

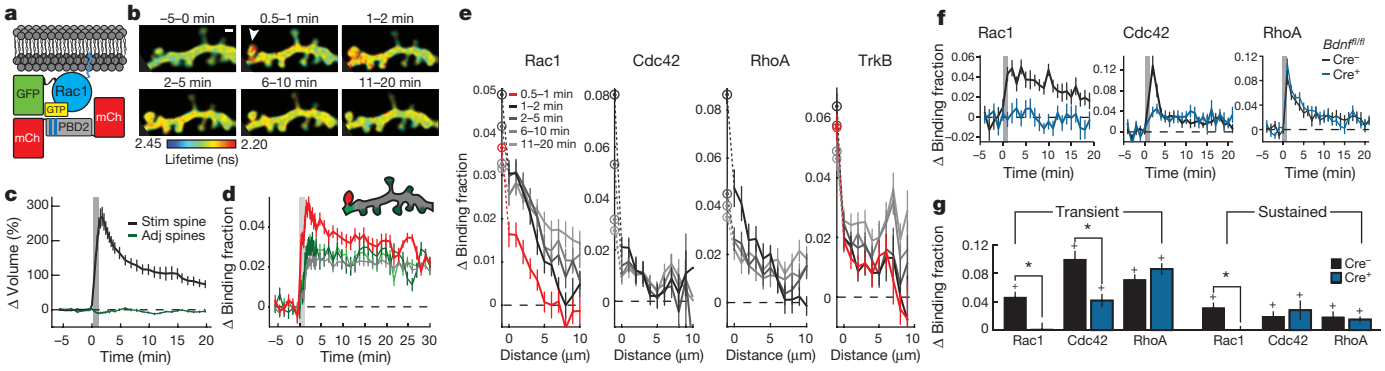

Figure 1 | The Rho GTPases Rac1 and Cdc42 convey postsynaptic BDNF–TrkB signalling across both homosynaptic and heterosynaptic domains. a, Schematic of Rac1 sensor. Monomeric enhanced green fluorescent protein (eGFP) is N-terminally tagged to Rac1 to preserve C-terminal membrane association. GTP binding leads to association with the Pak GTPase binding domain of PAK2^{R71C,S78A} (PBD2; blue lines denote mutations), bringing the mCherry (mCh) fluorophores within the FRET distance of eGFP, decreasing its fluorescence lifetime. **b**, Representative 2pFLIM images of Rac1 activation in dendrites during sLTP induced in a single spine with two-photon glutamate uncaging (white arrowhead). Scale bar, 1 μm. **c**, Time course of spine volume changes during sLTP induced with two-photon glutamate uncaging (grey window) in the stimulated spine (black) and compared to adjacent spines (green). $n = 102$ cells/121 spines. **d**, Time course of Rac1 activation during sLTP, measured as a change in the fraction of acceptor-bound eGFP–Rac1 in the stimulated spine (black), nearby spines (green), dendrite near the stimulated spine (cyan) and whole dendrite in the image (grey). $n = 102/121$ (cells/spines). **e**, Activations of Rac1 ($n = 56/79$), Cdc42 ($n = 25/38$), RhoA ($n = 21/23$), and TrkB ($n = 48/52$) (cells/spines) in dendrites as a function of distances from the base of the stimulated spines (lines) and in the stimulated spines (circles). **f**, Dependence of Rho GTPase activation on postsynaptically synthesized BDNF. Blue indicates co-expression of Cre recombinase in *Bdnf*$^{fl/fl}$ slices along with the Rac1 (left; $n = 7/13$ Cre$^-$, $n = 8/16$ Cre$^+$), Cdc42 (middle; $n = 5/12$ Cre$^-$, $n = 4/11$ Cre$^+$), or RhoA (right; $n = 6/13$ Cre$^-$, $n = 7/14$ Cre$^+$) (cells/spines) sensor. Black represents the corresponding control (Cre$^-$) data. **g**, Summary of data from **f**. Bars represent the average of the activation 1–2 min after stimulation. Error bars represent s.e.m. $^*P < 0.05$ (two-tailed *t*-test between groups); $^+P < 0.05$ (*t*-test compared to the baseline).

[1]Neurobiology Department, Duke University Medical Center, Research Drive, Durham, North Carolina 27710, USA. [2]National Institute for Physiological Science, Myodaiji, Okazaki, Aichi, 444-8585, Japan. [3]Max Planck Florida Institute for Neuroscience, 1 Max Planck Way, Jupiter, Florida 33458, USA. †Present address: Neurobiology Section, Center for Neural Circuits and Behavior, and Department of Neurosciences, University of California, San Diego, 9500 Gilman Drive, La Jolla, California 92093, USA.
*These authors contributed equally to this work.

Was Doggerland catastrophically flooded by the Mesolithic Storegga tsunami?

Jon Hill[*], Alexandros Avdis[**], Simon Mouradian[**], Gareth Collins[**] and Matthew Piggott[**,†]

[*]Environment Department, University of York, UK. jon.hill@york.ac.uk
[**]Earth Science and Engineering, Imperial College London, UK.
[†]Grantham Institute for Climate Change, Imperial College London, UK.

July 19, 2017

Abstract

Myths and legends across the world contain many stories of deluges and floods. Some of these have been attributed to tsunami events. Doggerland in the southern North Sea is a submerged landscape and is thought to have been heavily affected by a tsunami such that it was abandoned by Mesolithic human populations at the time of the event. The tsunami was generated by the Storegga submarine landslide off the Norwegian coast which failed around 8150 years ago. At this time there were also rapid changes in sea level associated with the deglaciation of the Laurentide ice sheet and drainage of its large proglacial lakes, with the largest sea level jumps occurring just prior to the Storegga event. The tsunami affected a large area of the North Atlantic and left sedimentary deposits across the region, from Greenland, through the Faroes, the UK, Norway and Denmark. From these sediments, run-up heights of up to 20 metres have been estimated in the Shetland Isles and several metres on mainland Scotland. However, sediments are not preserved everywhere and so reconstructing how the tsunami propagated across the North Atlantic before inundating the landscape must be performed using numerical models. These models can also be used to recreate the tsunami interactions with now submerged landscapes, such as Doggerland. Here, the Storegga submarine slide is simulated, generating a tsunami which is then propagated across the North Atlantic and used to reconstruct the inundation on the Shetlands, Moray Firth and Doggerland. The uncertainty in reconstructing palaeobathymetry and the Storegga slide itself results in lower inundation levels than the sediment deposits suggest. Despite these uncertainties, these results suggest Doggerland was not as severely affected as previous studies implied. It is suggested therefore that the abandonment of Doggerland was primarily caused by rapid sea level rise prior to the tsunami event.

1 Introduction

Global myths and 'traditional oral tales' contain many stories of great deluges or flooding events. A number of these have been attributed to tsunami inundation (Bryant et al. 2007, Heaton & Snavely 1985, Antonopoulos 1992) or sea level rise (Nunn 2014, Giosan et al. 2009) and an increasing body of geological evidence is being discovered to test the validity of the legends (Bruins et al. 2008). In the southern North Sea, the now submerged island of Doggerland was still emergent at around 8 kyr and was occupied by Mesolithic communities (Ballin 2017). Due to rising sea levels Doggerland was eventually flooded completely (Coles 1998). However, studies have hypothesised that Doggerland was inundated by a large tsunami caused by the Storegga submarine landslide which occurred around 8150 years ago (Bondevik et al. 2012), with some estimates of 5m high waves impacting the island (Hill et al. 2014). If true, this would have been a catastrophic event, affecting the communities living there, and possibly causing the abandonment of the island (Weninger et al. 2008). However, due to uncertainties in the relative timing of sea level rise events (Lawrence et al. 2016) and the magnitude of the Storegga tsunami on Doggerland (Hill et al. 2014), it has been challenging to untangle the effect of these events on Doggerland.

LIFESAVING

NUCLEAR FACTS AND SELF-HELP INSTRUCTIONS

NUCLEAR WAR SURVIVAL SKILLS

UPDATED AND EXPANDED
1987 EDITION

BY

CRESSON H. KEARNY

AUTHOR OF THE ORIGINAL 1979
OAK RIDGE NATIONAL LABORATORY
EDITION

FOREWORD
BY

DR. EDWARD TELLER

JULIAN JAYNES

THE ORIGIN OF **CONSCIOUSNESS** IN THE BREAK DOWN OF THE BICAMERAL MIND

MARINER BOOKS

TrussFab: Fabricating Sturdy Large-Scale Structures on Desktop 3D Printers

Robert Kovacs, Anna Seufert, Ludwig Wall, Hsiang-Ting Chen, Florian Meinel, Willi Müller, Sijing You, Maximilian Brehm, Jonathan Striebel, Yannis Kommana, Alexander Popiak, Thomas Bläsius, and Patrick Baudisch
Hasso Plattner Institute, Potsdam, Germany
{firstname.lastname}@hpi.uni-potsdam.de

ABSTRACT
We present *TrussFab*, an integrated end-to-end system that allows users to fabricate large scale structures that are sturdy enough to carry human weight. TrussFab achieves the large scale by complementing 3D print with plastic bottles. It does not use these bottles as "bricks" though, but as beams that form structurally sound node-link structures, also known as *trusses*, allowing it to handle the forces resulting from scale and load. TrussFab embodies the required engineering knowledge, allowing non-engineers to design such structures and to validate their design using integrated structural analysis. We have used TrussFab to design and fabricate tables and chairs, a 2.5 m long bridge strong enough to carry a human, a functional boat that seats two, and a 5 m diameter dome.

Author Keywords
Fabrication; 3D printing; truss structure.

ACM Classification Keywords
H5.2 [Information interfaces and presentation]: User Interfaces: Input Devices and Strategies, Interaction Styles.

INTRODUCTION
Personal fabrication tools, such as 3D printers have become popular in HCI, where they have been used for fast prototyping [20] as well as to fabricate interactive objects [9], optical elements [34], or kinematic characters [5]. Since 3D printers today are available in a desktop form factor, they have been able to spread to the maker community [30] and are now increasingly reaching the consumer market [27].

In contrast, the fabrication of *large* objects still has remained a privilege of industry, which has access to specialized equipment, such as concrete printers that allow making houses [13] or robotic-arms capable of 3D printing [11]. The owners of the widespread desktop devices, in contrast, cannot participate in this evolution, because the underlying technology does not scale. Even techniques that break down large models into printer-sized parts [16] ultimately do not scale, as large models consume material and time proportional to their size, which quickly renders 3D printing and related techniques intractable for larger-than-desktop-scale models.

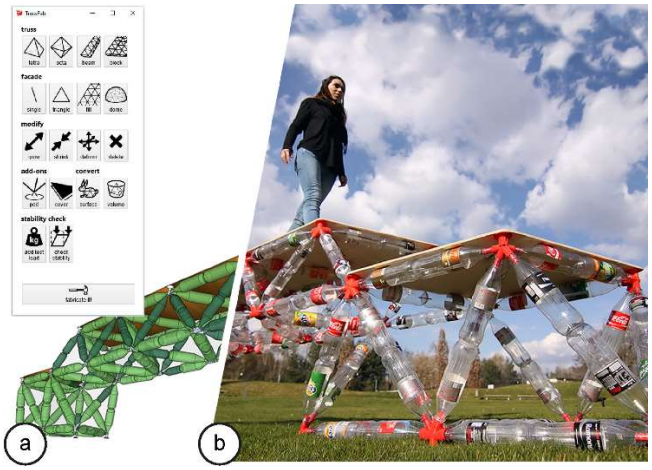

Figure 1: *TrussFab* is a system that allows users to fabricate large structures sturdy enough to carry human weight. TrussFab considers bottles as beams that form structurally sound node-link structures also known as *trusses*, allowing it to handle the forces resulting from scale and load.

As an alternative approach, fabrication enthusiasts have created large objects by combining 3D print with ready-made objects, such as plastic bottles [39]. In their simplest form, such objects wrapped in 3D print can serve as 3D voxel collages that approximate the volume of an object [36].

Going larger, however, is not only about scale and print volume. For large objects, the main design objective is typically to withstand large forces, as forces grow cubed with the size of the object. Also, large objects afford substantial external loads; furniture, bridges, and vehicles, for example, all must be engineered to hold the weight of a human. Designing for large forces, however, requires substantial engineering skill [40] from envisioning appropriate structures in the first place to verifying their structural integrity.

In this paper, we present *TrussFab*, an integrated end-to-end system that allows users to design large structures that are sturdy enough to carry human weight (Figure 1). TrussFab achieves this by taking a different perspective on bottles. Unlike previous systems that stacked bottles as if they were "bricks", TrussFab considers them as beams and uses them

Authors' copy.
Published in Proceedings of CHI '17, May 6 - 11, 2017, Denver, USA

TID-7695

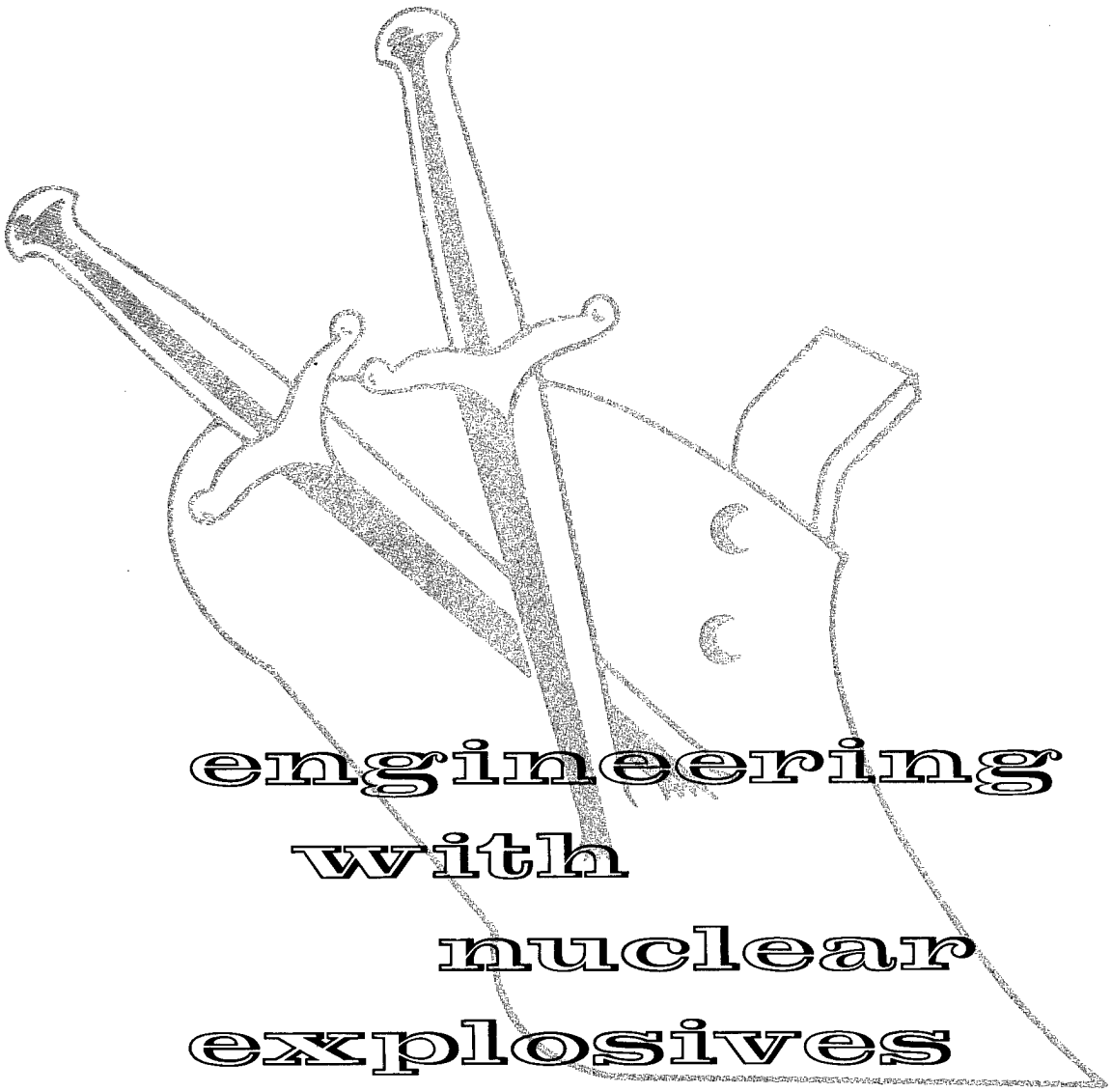

engineering with nuclear explosives

PROCEEDINGS OF THE THIRD PLOWSHARE SYMPOSIUM

U.S. ATOMIC ENERGY COMMISSION / Division of Technical Information

Research Article | Vol. 25, No. 2 | 23 Jan 2017 | OPTICS EXPRESS 1221

Optics EXPRESS

Tunable-focus lens for adaptive eyeglasses

NAZMUL HASAN,* AISHWARYADEV BANERJEE, HANSEUP KIM, AND CARLOS H. MASTRANGELO

Department of Electrical and Computer Engineering, University of Utah, Salt Lake City, Utah 84112, USA

nazmul.hasan@utah.edu

Abstract: We demonstrate the implementation of a compact tunable-focus liquid lens suitable for adaptive eyeglass application. The lens has an aperture diameter of 32 mm, optical power range of 5.6 diopter, and electrical power consumption less than 20 mW. The lens inclusive of its piezoelectric actuation mechanism is 8.4 mm thick and weighs 14.4 gm. The measured lens RMS wavefront aberration error was between 0.73 µm and 0.956 µm.

OCIS codes: (220.1080) Active or adaptive optics; (220.3620) Lens system design.

References and links

1. W. Tasman and E. A. Jaeger, *Duane's Ophthalmology* (LLW, 2013).
2. M. P. Keating, *Geometric, Physical and Visual Optics* (Butterworth-Heinemann, 2002).
3. S. H. Schwartz, *Geometrical and Visual Optics* (McGraw-Hill, 2002).
4. D. A. Goss and R. W. West, *Introduction to the Optics of the Eye* (Butterworth- Heinemann, 2001).
5. S. Resnikoff, D. Pascolini, S. P. Mariotti, and G. P. Pokharel, "Global magnitude of visual impairment caused by uncorrected refractive errors in 2004," Bull. World Health Organ. **86**(1), 63–70 (2008).
6. C. E. Letocha, "The invention and early manufacture of bifocals," Surv. Ophthalmol. **35**(3), 226–235 (1990).
7. L. Johnson, J. G. Buckley, A. J. Scally, and D. B. Elliott, "Multifocal spectacles increase variability in toe clearance and risk of tripping in the elderly," Invest. Ophthalmol. Vis. Sci. **48**(4), 1466–1471 (2007).
8. S. R. Lord, J. Dayhew, and A. Howland, "Multifocal glasses impair edge-contrast sensitivity and depth perception and increase the risk of falls in older people," J. Am. Geriatr. Soc. **50**(11), 1760–1766 (2002).
9. T. Callina and T. P. Reynolds, "Traditional methods for the treatment of presbyopia: spectacles, contact lenses, bifocal contact lenses," Ophthalmol. Clin. North Am. **19**(1), 25–33 (2006).
10. H. Ren and S.-T. Wu, *Introduction to Adaptive Lenses* (Wiley, 2012).
11. H. Jiang and X. Zeng, *Microlenses: Properties, Fabrication and Liquid Lenses* (CRC Press, 2013).
12. L. Alvarez, "Two-element variable power spherical lens," U.S. Patent Application 3305294 (1967).
13. L. W. Alvarez, "Development of variable- focus lenses and a new refractor," J. Am. Optom. Assoc. **49**(1), 24–29 (1978).
14. O. Aves, "Improvements in and relating to multifocal lenses and the like, and the method of grinding same," GB patent no. 15735 (1908).
15. C.-P. Chiu, T.-J. Chiang, J.-K. Chen, F.-C. Chang, F.-H. Ko, C.-W. Chu, S.-W. Kuo, and S.-K. Fan, "Liquid lenses and driving mechanisms: A review," J. Adhes. Sci. Technol. **26**(12), 1773–1788 (2012).
16. H. Ren, D. Fox, P. A. Anderson, B. Wu, and S.-T. Wu, "Tunable-focus liquid lens controlled using a servo motor," Opt. Express **14**(18), 8031–8036 (2006).
17. F. Carpi, G. Frediani, S. Turco, and D. De Rossi, "Bioinspired tunable lens with muscle-like electroactive elastomers," Adv. Funct. Mater. **21**(21), 4152–4158 (2011).
18. S. Shian, R. M. Diebold, and D. R. Clarke, "Tunable lenses using transparent dielectric elastomer actuators," Opt. Express **21**(7), 8669–8676 (2013).
19. M. Niklaus, S. Rosset, and H. Shea, "Array of lenses with individually tunable focal-length based on transparent ion implanted EAPs," Proc. SPIE **7642**, 76422K (2010).
20. N. Hasan, H. Kim, and C. H. Mastrangelo, "Large aperture tunable-focus liquid lens using shape memory alloy spring," Opt. Express **24**(12), 13334–13342 (2016).
21. H. Ren and S.-T. Wu, "Variable-focus liquid lens by changing aperture," Appl. Phys. Lett. **86**(21), 211107 (2005).
22. N. Peyghambarian, G. Li, and P. Ayras, "Adaptive electro-active lens with variable focal length," U.S. patent application 0164593 (2006).
23. C. W. Fowler and E. S. Pateras, "Liquid crystal lens review," Ophthalmic Physiol. Opt. **10**(2), 186–194 (1990).
24. A. Naumov, G. Love, M. Yu. Loktev, and F. Vladimirov, "Control optimization of spherical modal liquid crystal lenses," Opt. Express **4**(9), 344–352 (1999).
25. H. Ren, D. W. Fox, B. Wu, and S.-T. Wu, "Liquid crystal lens with large focal length tunability and low operating voltage," Opt. Express **15**(18), 11328–11335 (2007).
26. S. Sato, "Applications of liquid crystals to variable-focusing lenses," Opt. Rev. **6**(6), 471–485 (1999).

#280750 http://dx.doi.org/10.1364/OE.25.001221
Journal © 2017 Received 15 Nov 2016; revised 19 Dec 2016; accepted 24 Dec 2016; published 17 Jan 2017

This article has been accepted for publication in a future issue of this journal, but has not been fully edited. Content may change prior to final publication. Citation information: DOI 10.1109/TAP.2015.2435037, IEEE Transactions on Antennas and Propagation

A High Power Microwave Zoom Antenna with Metal Plate Lenses

J. Lawrance, C. Christodoulou, M. R. Taha

***Abstract*—Metal plate lens antennas were designed and constructed for a high power microwave zoom antenna concept comprising a pyramidal horn feed antenna and two metal plate lenses. Good agreement was found between experiment and simulation. This antenna provides true zoom capability with continuously variable collimated beam output, approximately 10% bandwidth, and very high power handling capability. It can be designed to operate at any frequency in the range of about 100MHz to 10GHz. It was found that nano-modified carbon fiber composites could be used instead of metal plates in these lenses; these composites would reduce the weight of the lens significantly and would help to mitigate possible spurious TM modes induced in the lens when it is in the near field of the feed horn antenna.**

***Index Terms*—Zoom antennas, metal plate lenses, parallel plate waveguide lenses, high power microwave zoom antenna**

I. INTRODUCTION

A true zoom antenna produces a collimated beam of electromagnetic (EM) energy with a planar wavefront and with continuously variable diameter. This type of antenna provides beam control in terms of spot size and power density on target. A true high power microwave (HPM) zoom antenna greatly extends the range of an HPM source and is useful for such applications as target acquisition and tracking, and communications. Until now, true zoom antenna capability for high power microwave applications did not exist.

The zoom antenna concept presented herein and in [1] consists of a horn feed antenna and two metal plate lenses. These lenses are particularly well suited to this application. While aluminum was originally the metal of choice for these lenses, newly emerging carbon fiber reinforced polymer (CFRP) composites were demonstrated in simulation to have sufficient conductivity for this application and bear further study. These compounds have lower density than aluminum; they provide a lightweight alternative to metal for lens construction, which becomes important for applications at lower frequencies

This effort comprised design and demonstration – through experiment and simulation - of a true zoom antenna concept for HPM applications. This is a narrowband antenna with approximately 10% bandwidth which produces a linearly polarized collimated beam with continuously variable diameter (achieved by axial translation of the lenses relative to each other and relative to the feed horn). The zoom antenna can be designed for a wide range of frequencies from hundreds of megahertz (MHz) to tens of gigahertz (GHz). It has excellent power handling capability: ranging from tens of megawatts (MW) at 10GHz to several gigawatts (GW) at 1GHz.

This is a practical system that could be implemented in the field near-term. Design considerations and analysis are focused on minimizing complexity and cost of fabrication. However, if minimizing weight is an issue, carbon fiber compounds should be considered for lens construction.

II. BACKGROUND

Historically, the term "zoom antenna" has been erroneously applied to reflector antennas that are used to broaden the beam through a defocusing effect; there are a number of these types of antennas described in available literature and existing patents; some examples are given in [2-4]. These are not technically zoom antennas. While Cassegrain and Gregorian (reflector) antennas can produce a collimated beam of electromagnetic energy; they cannot provide continuously variable diameter of this collimated beam. True zoom capability cannot be achieved with any of these reflector type antennas.

A true high power microwave (HPM) zoom antenna therefore requires the use of lenses. Dielectric lenses are not a good option for HPM applications because they are lossy at high frequencies and because they become prohibitively heavy at lower frequencies on the order of a few gigaherz. Metal plate lenses are particularly well-suited to the HPM zoom antenna application.

The concept of the metal plate lens was proposed by W.E. Kock [5] in the 1940's; however, it has found limited application since. More detailed discussion of these lenses is found in [6-9]. According to Kraus, [10], one of the major benefits of parallel plate waveguide lenses (or what he refers to as "E-plane metal plate lens antennas") over parabolic reflectors is that the tolerance of this type of lens is much higher than the surface contour requirements of a parabolic reflector such that, "a relatively large amount of warping and twisting can be tolerated". This is a major benefit for a practical system that can be implemented in the field, and, in fact, this was demonstrated to be true in experiments presented herein.

A drawback of these lenses, according to Kraus, is their small bandwidth. He derives in [6] a bandwidth on the order of 5% [10]; however, this is based on an arbitrarily chosen value

A 800- to 3200-MHz Wideband CPW Balun Using Multistage Wilkinson Structure

*Jong-Sik Lim[O], **Ung-Hee Park, *Sungmin Oh, *Jae-Jin Koo, ***Yong-Chae Jeong, and *Dal Ahn

*Division of Information Technology Engineering, Soonchunhyang University, Rep. Of KOREA
** Electronics and Telecommunications Research Institute, Rep. Of KOREA
***Division of Electronics and Information Engineering, Chonbuk National University, Rep. Of KOREA

Abstract **— A novel ultra-wide band CPW(Coplanar Waveguide) balun having the structure of multistage Wilkinson power divider is proposed. It has an 180° phase inverting structure between signal line and ground planes of CPW transmission line. The 3-stage Wilkinson power divider is transformed directly into the ultra-wide band balun without any cost of the size and performances. The measurement shows the right S-parameters as a power divider and the proper out of phase as a balun. The measured amplitude and phase unbalances at output ports are ± 0.5dB and ± 6°, respectively over 800~3200MHz, while the maximum insertion loss is 0.8dB.**

Index Terms **— Wilkinson dividers, baluns, CPW, coplanar waveguide.**

I. Introduction

One of widely used applications in wireless-related circuits and systems such as antenna, receivers(or mixers), high power amplifiers, and antenna measurement facilities is the power dividing into two output ports with out of phase characteristic, or vice versa. Baluns are used to perform these functional goals. There have been a lot of types of balun, and even recently many new balun topologies are proposed. Out of lots of balun circuit, baluns having the Wilkinson structure (hereinafter "Wilkinson balun") are popular because of simple structure and design, familiarity, and expandability to new application and so on.

Wilkinson divider is greatly extensively used not only as a basic power divider, but various modified power dividers/baluns[1,2]. Because the basic single stage Wilkinson divider has narrow band performances, multi-stage topologies are required for wide band operations. For example, a 3-stage Wilkinson divider guarantees at least octave bandwidth, which means "F_{low}:F_{high}=1:3" [3-5].

By the way when a wide band Wilkinson divider has been realized using CPW (Coplanar Waveguide) elements and if the structural advantage of CPW elements well taken of, it is possible to design an ultra wide band balun having the Wilkinson structure without any cost of size and performance by inserting an 180° phase inverting. The proposed balun in this paper does not require any additional area to form the balun circuit from Wilkinson divider, and holds the performances as a power divider plus to the out of phase characteristic at output ports.

II. Multi-stage Wideband Wilkinson Divider

Wilkinson dividers have simple structure and their applicability is excellent, so they are used for other purposes like balun as well as for inherent power divider. A basic Wilkinson power divider has two in-phase output ports. This means that additional circuit elements should be added to output ports for out of phase characteristic in order to be used as a balun.

However the single stage Wilkinson divider has a relatively narrow bandwidth. Fig. 1 shows the ideal performances of a single stage Wilkinson divider calculated on Agilent Advanced Design System. When -25dB of isolation (S32) between output ports is taken as the criterion of bandwidth, the ideally achieved bandwidth is only 20%. Even though the criterion is mitigated to -15dB of S32, the bandwidth is 50% only.

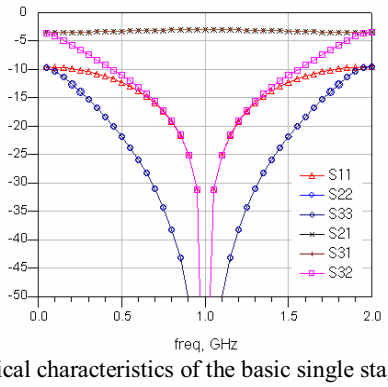

Fig 1. Theoretical characteristics of the basic single stage Wilkinson power divider

A good method to extend the bandwidth is to design a multistage Wilkinson divider. If 100% of fractional bandwidth (FBW) is required, at least 3-stage is chosen because "F_{low}:F_{high}=1:3"[3-5]. Fig. 2 shows the ideal performances of the 3-stage Wilkinson divider. As described just now, more

0-7803-9542-5/06/$20.00 ©2006 IEEE

MODERN ANTENNA HANDBOOK

Edited by

Constantine A. Balanis

WILEY

A JOHN WILEY & SONS, INC., PUBLICATION

REFLECTARRAY ANTENNAS

130MHz lower freq.

Disc

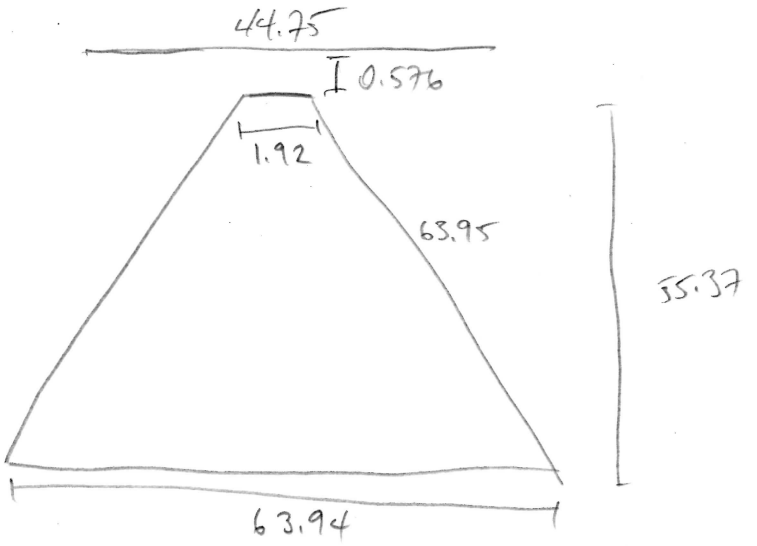

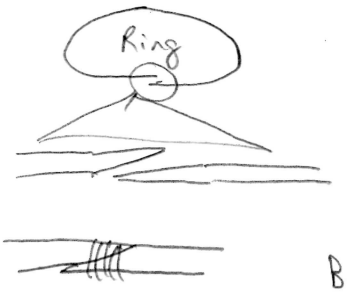

Flatten ends.

Bind ends with copper wire & Solder.

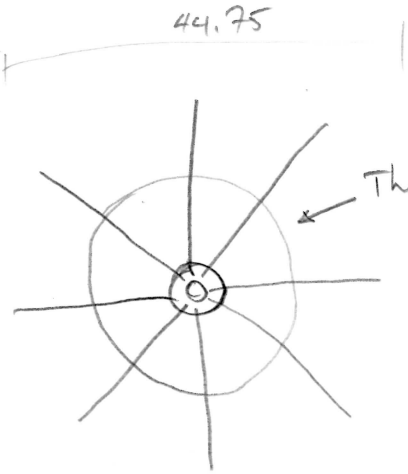

This ring is arbitrary size
Just a support for the spokes

At the join use solid copper wire stripped from ethernet cable to attach. ~~the~~
by tightly looping then twist the ends.

~~At~~ At the washer ~~hap~~ hammer the ends of the gal wire to flatten them & make them easier to solder to the washer.

When soldering to gal. steel, sand the galvinisation to clean it then use liberal flux & a lot of heat >100w.

This article has been accepted for publication in a future issue of this journal, but has not been fully edited. Content may change prior to final publication. Citation information: DOI 10.1109/TAP.2014.2334358, IEEE Transactions on Antennas and Propagation

Simply-Fed Four-Arm Spiral-Helix Antenna

Mohamed A. Elmansouri, James B. Bargeron, and Dejan S. Filipovic

***Abstract*— An ultra-wideband four-arm spiral-helix antenna with simple beamformer is developed to have simultaneously good performance in time and frequency. Two microstrip feeds printed on the opposite side of the spiral with impedance following Klopfenstein taper are employed to eliminate the need for 180° hybrids used in conventional beamformers. Ferrite beads placed around the coaxial cables connected between the ground and microstrip are utilized to choke unbalanced currents and prevent shorting the spiral aperture to the ground. Helix is used to improve the low-frequency performance and allow easy attachment of resistive loading to the ground plane. A metallic inset is placed inside the cavity to eliminate the destructive pattern interference and improve the high-frequency gain. To achieve low dispersion, the spiral is loosely wrapped. Simultaneously good time and frequency domain performance from 0.5GHz to 3GHz with VSWR<2, nominal gain and radiation efficiency of 6dBic and 80%, respectively, broadside axial ratio below 1.8dB and fidelity factor of 93% over wide field of view are demonstrated in simulations and experiments.**

***Index Terms*— Fidelity factor, four-arm spiral antenna, spiral-helix antenna, time-domain.**

I. Introduction

Four-arm spiral antennas are known for multi-mode capability and superior frequency-domain performance compared to their two-arm spiral counterparts [1]. The detailed modal analysis in [2] showed that the multiple arms act as modal filter that eliminates the radiation of undesired modes, thus enabling the four-arm spiral to achieve very low axial ratio and high pattern purity over wide bandwidth and field of view. In addition, loosely wrapped four-arm spirals may achieve simultaneously good frequency-domain radiation and very low-dispersion [3] thus extending their candidacy for applications needing antennas with simultaneously good time and frequency responses. However, two issues remain, specifically, the efficiency and the complexity of the feed network. Both shortcomings are overcome in this work. Experiments and simulations are used to verify the improvements in frequency- and time-domain responses compared to the more conventional designs.

To achieve unidirectional and consistent patterns with planar spirals they are typically backed by an absorber. This reduces antenna's gain for 3dB or more with nominal total efficiency falling under 50%. The use of metallic backing with a conventional spiral without any treatment of arms [4]-[6] or cavity [6]-[8] deteriorates significantly the impedance match and the far-field performance when multiple octave bandwidths are desired for their use.

A viable approach to maintain good frequency-domain performance with a metallic backing is to terminate the spiral's arms with quadrifilar helix having attached lumped resistors at its bottom end. This approach is discussed in [9] wherein the benefits of using the helix termination to improve the four-arm spiral's low-end gain and eliminate circular cavity modes are demonstrated. To make the four-arm spiral-helix antenna more practical, the complexity of the beamformer needs to be reduced. In this paper, the main objective is to reduce the complexity of antenna's beamformer and thus allow for a four-arm spiral antenna to be a serious contender to the more established two-arm configuration for many commercial and defense applications. Specifically, a combined embedded coaxial / planar tapered dual-microstrip feeding arrangement is proposed to mitigate the issues associated with the mode 1 beamforming of a four-arm spiral-helix antenna while maintaining good time-domain and frequency-domain performances over at least 6:1 bandwidth. Microstrip feed is designed to perform impedance transformation and 180° phase offset between the sets of opposite arms in a similar way as shown with a two-arm spiral from [10]. This way, the need for the 2nd row of the modified Butler matrix beamformer [1]-[2] composed of two 180° hybrids is eliminated. The microstrip ground at the taper's outside end is used to solder the shield of a coaxial cable which routes the signal under the antenna ground plane into a 90° hybrid needed to establish the required mode 1 phasing. To prevent shorting of the aperture to the ground, a row of ferrite beads wrapped around coaxial cables is placed between the coax-to-microstrip transition and cavity bottom. Over the considered 0.5-3GHz bandwidth, the fabricated antenna has measured fidelity factor >90%, VSWR <2, axial ratio < 1.8dB, high efficiency, and consistent patterns with nominal gain of 6dBic. Good agreement with theory verifies the quality of prototyping and soundness of the proposed design principles.

II. Antenna Description

A conventional beamformer for a mode 1 four-arm spiral has two 180° and one 90° hybrid as shown in Fig. 1(a). While a decade bandwidth components are available, they are expensive, bulky, and lossy with higher imbalances that negatively impact the antenna performance. In addition, the internal port of 180° hybrid must be terminated which altogether brings forth the need for a beamformer housing further increasing the cost, design and platform integration challenges. To reduce the complexity of the feed network, a planar microstrip feed is developed as shown in Fig. 1(b). The designed microstrip feed has a spiral shape and it is based on Klopfenstein impedance taper [10] that transforms 50Ω impedance at the input of the coaxial feed to 140Ω at the center of the spiral. The metallic spiral arms act as a ground plane for the two microstrip lines. The above described planar microstrip impedance transformers are used to feed the two sets of opposite arms of the antenna thus achieving the required 180°

Manuscript received March 11, 2014. This work is sponsored by the Office of Naval Research (ONR) award #N00014-10-C-0467.

M. Elmansouri, J. Bargeron, and D. S. Filipovic are with the Department of Electrical, Computer, and Energy Engineering, University of Colorado, Boulder, CO 80309-0425 USA (e-mail: dejan.filipovic@colorado.edu).

This article has been accepted for publication in a future issue of this journal, but has not been fully edited. Content may change prior to final publication. Citation information: DOI 10.1109/TAP.2015.2429733, IEEE Transactions on Antennas and Propagation

Design of a wideband horizontally polarized omnidirectional antenna with mutual coupling method

ZeDong Wang, YingZeng Yin, Xi Yang and JianJun Wu

***Abstract*—A wideband horizontally polarized (HP) omnidirectional antenna is proposed in this communication, which consists of 12 printed arc dipole units, a wideband 1to12 feed network, two rows of parasitic arc strips and a row of director elements. Based on the tightly coupled dipole array design, twelve printed arc dipoles (about $0.2\lambda_L$, λ_L: effective wavelength at low frequency) are formed as a ring with their edge overlap for strong mutual coupling. Meanwhile, the two rows of parasitic arc strips are radially placed around these arc dipoles as an impedance matching layer. Owing to the strong mutual coupling and impedance matching layer, the proposed HP omnidirectional antenna has a wideband operating band. Additionally, a row of director elements is utilized to enhance the radiation in horizontal plane. The printed arc dipoles are fed by a wideband 1to12 power divider with identical magnitude and phase. Experimental results show that this antenna has a wide 10-dB return loss operating bandwidth of 70.2% (1.7~3.54GHz) and good omnidirectionality performance with gain variation in horizontal plane being less than 1.2dB among 1.7~3.2GHz.**

***Index Terms*—Horizontal polarization, omnidirectional antenna, wideband, mutual coupling.**

I. INTRODUCTION

Omnidirectional antenna has been greatly applied in wireless communications systems for 360° coverage. In most indoor and urban environment, the vertically polarized omnidirectional antenna is always used. For increasing the capacity of system, the horizontally polarized (HP) omnidirectional antenna is an essential complement. Owing to development of modern wireless communication system, it induces the requirement of broadband antenna for covering multiple communication bands such as second generation (2G) systems, third generation (3G) system and long term evolution (LTE) system. In order to simultaneously operate in 2G/3G/LTE applications, the omnidirectional antenna must have a wide operating bandwidth of 45.5 %(1.7~2.7GHz). The wideband vertically polarized omnidirectional antenna can be easily obtained by suitable design of monopole [1], [2]. However, it is more challenging to design a wideband HP omnidirectional antenna.

Many literatures have been published in [3]-[9] to obtain an HP omnidirectional antenna. Based on the rotating field method, the turnstile antennas [3], [4] consist of cross dipoles in horizontal plane, which are fed in phase quadrature to achieve omnidirectional horizontal polarization. But these two turnstile antennas have a narrow operating bandwidth about 12.2 % (2.3~2.6GHz). According to the theory of magnetic dipole, the common method to design an HP omnidirectional antenna is to construct a small loop antenna with uniform current distribution. As we all know, the small loop antenna has small radiation resistance and high reactance, which make it difficult to be matched [10]. The loop antenna with large diameter has a reasonable impedance performance. However, it is difficult to ensure the uniform current distribution on the large loop to have a small gain variation in horizontal plane. Meanwhile, the large diameter of loop antenna would make its main radiating direction being off the horizontal plane. Alford loop antennas [5], [6] are proposed to obtain a HP omnidirectional radiation. Four arc dipoles with length about $\lambda/2$ (λ: wavelength in free space at center frequency) construct as a loop antenna. A 1to4 power divider is used to feed these four arc dipole. The Alford loop antenna [5] has a 10-dB return loss (RL) operating bandwidth of 27.1% (1.69~2.22GHz) with a gain variation of 1.5dB in the horizontal plane. A large operating bandwidth of 41 %(1.76~2.68GHz) for RL>10dB is obtained in [6]. But undesirable radiation performance in horizontal plane occurs at high operating frequency because the current is non-uniformly distributed on each arc dipole. In [7], [8], the artificial mu-negative transmission line is utilized in loop antenna to maintain the current on loop in phase for HP omnidirectional radiation. The loop antenna [7] has a narrow operating band 2.32~2.58GHz, while a wider operating band 2.17~2.97GHz is obtained in the antenna [8] with its performance of gain variation becoming worse at high operating frequency. A broadband four magneto-electric antenna array [9] is arranged as a ring to obtain an HP omnidirectional radiation. This antenna has a 38% impedance bandwidth. But its maximum radiating direction is not in horizontal plane. Through the discussion of the previous HP omnidirectional antenna designs, it can be found that it is difficult to design an HP omnidirectional antenna which simultaneously owns a large operating bandwidth over 40% and good gain variation performance among whole operating band.

In recent years, many wideband dipole array designs based on tight coupling mechanism [11]-[16] have been published. The wide bandwidth of tightly coupled phased arrays is attributed to the strong inter-element coupling. The current distribution on elements effectively emulates a sheet of uniform current [17] proposed by wheeler. Through strong inter-element capacitive coupling, these phased dipole arrays can own a very broad operating bandwidth over 100%.

In this communication, a wideband HP omnidirectional antenna is presented. Inspired by the design of tightly coupled dipole array, twelve printed arc dipoles ($0.2\lambda_L$, λ_L: effective wavelength at low frequency) are designed with edge overlap for strong inter-element capacitive coupling. They are formed as a loop and fed by a 1to12 wideband power divider with equal magnitude and identical phase to create a good HP omnidirectional radiation. Moreover, two rows of arc parasitic

This work is supported by Basic Science Research Fund in Xidian University(K5051202040)

Z.D. Wang, Y.Z. Yin, X. Yang and J.J. Wu are with National Key Laboratory of Antennas and Microwave Technology, the School of Electronic Engineering, Xidian University, Xi'an, 710071, China. (Email:zedongwang1989@163.com).

A Compact, Capacitively-Fed UWB Antenna With Monopole-Like Radiation Characteristics

Mingjian Li, *Member, IEEE,* and Nader Behdad, *Fellow, IEEE*

***Abstract*—A compact, ultra-wideband (UWB) antenna occupying a cylindrical volume and providing omni-directional monopole-like radiation is introduced. The antenna consists of two closely-placed three-dimensional (3D) loops, two parasitic small loops, and a circular top hat. Two strip-shaped probes, each coupling with one loop, are used to feed the antenna in common mode. UWB operation is achieved by taking advantage of the magnetic coupling of the parallel-fed 3D loops. Small electrical dimensions of the antenna are due to the special capacitive proximity feeding scheme and the presence of the top hat. A prototype with 4.1:1 bandwidth is designed, fabricated, and characterized. The antenna demonstrates a VSWR better than 2:1 and monopole-like omni-directional radiation characteristics across this entire band. It occupies a cylindrical volume with a diameter of 0.14λ_{min} and a height of 0.09λ_{min}, where λ_{min} is the free-space wavelength at the lowest frequency of operation. The antenna has a $k_{min}a = 0.73$, where k_{min} is the wavenumber at its lowest frequency of operation. The fabricated prototype is demonstrated to have a lowest frequency of operation that is only 10% above the theoretical limits on UWB antennas. Further miniaturization of the antenna using a spherical top hat is also examined and demonstrated to be capable of reducing $k_{min}a$ values down to 0.60.**

***Index Terms*—Broadband antennas, electrically small antennas, ultrawideband antennas, omnidirectional antennas.**

I. Introduction

ULTRAWIDEBAND (UWB) technology has many applications in wireless communications and sensing systems ranging from ground penetrating radars and high data rate short-range wireless networks to civilian and military communications systems [1]. UWB antennas are critical parts of any UWB wireless systems. The design of a UWB antenna becomes very challenging for systems operating at the lower RF/microwave frequencies. This is due to the fact that the wavelength is very large at these frequencies and generally having physically large antennas is not desirable due to space limitations. This problem is particularly severe in military communications systems that operate at HF, VHF, and UHF bands because in such applications, having antennas with low visual signatures is of paramount importance. Such antennas are generally required to radiate vertically-polarized waves with omni-directional radiation patterns similar to a monopole antenna. The current antennas of choice for these applications tend to be monopole whip antennas used in conjunction with automatic impedance tuners [2]. These antennas, however, suffer from two major drawbacks. The first drawback is the relatively large heights of a conventional monopole whip antenna. When mounted on a vehicle, such an antenna significantly protrudes from the top surface of the vehicle drastically increasing the visual signature of the vehicle. The second issue with monopole whip antennas is their narrow bandwidths which limits the types of waveforms that they can receive or transmit. Therefore, development of compact, low-profile, and ultra-wideband antennas is of particular interest in many communications systems that operate at HF, VHF, and UHF frequencies.

In the past several decades, considerable efforts have been devoted to conducting research on investigating the fundamental limitations of electrically-small antennas as well as designing antennas providing performance levels close to these fundamental limitations. Since Wheeler [3] and Chu [4] derived the well-known theoretical limits on the performances of electrically-small antennas, a number of designs have been reported that approach these fundamental limits. A rather comprehensive survey of these antennas is provided in [5], where the performances of the most promising designs in this area are compared against the theoretical limits derived by Chu. Several specific examples of innovative designs for small antennas whose performances are compared in [5] include linear helix [6], spherical electric [7] and magnetic [8] dipoles, dual-mode spherical dipoles [9], miniaturized monopoles [10], [11], metamaterial inspired [12], and dielectric resonator [13] antennas. Among these antennas, the spherical electric and magnetic dipole antennas have performance levels that nearly approach the fundamental limits predicted by Chu. However, the bandwidth provided by these antennas is still not sufficient to meet the stringent demands of many UWB systems.

To increase the bandwidth of monopole-type radiators, a number of different techniques have been examined. A variety of printed monopole antennas that provide UWB operation in a planar form factor are examined in the 3.1-10.6 GHz band [14]–[16]. However, at its lowest frequency of operation, a printed monopole tends to have relatively large dimensions. Specifically, most printed monopole antennas have $k_{min}a$ values larger than 1, where k_{min} is the wavenumber at the lowest frequency of operation of the antenna and a is the radius of the smallest sphere that circumscribes the antenna. Thus scaling these designs to HF-UHF frequencies results

This material is based upon work supported by the Office of Naval Research under ONR Award No. N00014-15-1-2207 and Award No. N00014-16-1-2098. The authors are with the Department of Electrical and Computer Engineering, University of Wisconsin-Madison, Madison, WI, 53706 USA (e-mail: mli454@wisc.edu and behdad@wisc.edu)

Improvements in CPU & FPGA Performance for Small Satellite SDR Applications

Mamatha R. Maheshwarappa, *Student Member, IEEE*, Mark D. J. Bowyer, *Member, IEEE* and Christopher P. Bridges, *Member, IEEE*

***Abstract*— The ongoing evolution in constellation/formation of CubeSats along with steadily increasing number of satellites deployed in Lower Earth Orbit (LEO), demands a generic reconfigurable multimode communication platforms. As the number of satellites increase, the existing protocols combined with the trend to build one control station per CubeSat become a bottle neck for existing communication methods to support data volumes from these spacecraft at any given time. This paper explores the Software Defined Radio (SDR) architecture for the purposes of supporting multiple-signals from multiple-satellites, deploying mobile and/or distributed ground station nodes to increase the access time of the spacecraft and enabling a future SDR for Distributed Satellite Systems (DSS). Performance results of differing software transceiver blocks and the decoding success rates are analysed for varied symbol rates over different cores to inform on bottlenecks for Field Programmable Gate Array (FPGA) acceleration. Further, an embedded system architecture is proposed based on these results favouring the ground station which supports the transition from single satellite communication to multi-satellite communications.**

***Index Terms* — Central Processing Unit (CPU), Field Programmable Gate Array (FPGA), Satellite communication, Software Defined Radio (SDR), System-on-chip (SoC).**

I. Introduction

SMALL satellites are fast becoming a way to perform scientific and technological missions more affordably due to reduced build time, more frequent launch opportunities, larger variety of missions, more rapid expansion of the technical and/or scientific knowledge base and greater involvement of small industries/universities [1, 2]. Furthermore, there is an ongoing evolution of multiple small satellite scenarios such as FLOCK-1 [3], QB50 [4], Autonomous Assembly of a Reconfigurable Space Telescope (AAReST) [5], Surrey Training Research and Nano-Satellite Demonstrator (STRaND -2) [6] and Edison Demonstration of Smallsat Network (EDSN) [7]. The objectives of these missions are very ambitious and are driven by new complexities which require multi-mode operation of wireless transceivers [8].

This paragraph of the first footnote will contain the date on which you submitted your paper for review. It will also contain support information, including sponsor and financial support acknowledgment. For example, "This work was supported in part by the U.S. Department of Commerce under Grant BS123456".

M. R. Maheshwarappa and C. P. Bridges are with the Surrey Space Centre, Faculty of Engineering and Physical Sciences (FEPS), University of Surrey, Guildford, United Kingdom - GU27XH (e-mail: m.maheshwarappa@surrey.ac.uk; c.p.bridges@surrey.ac.uk).

M. D. J. Bowyer is with Airbus Defence and Space Ltd., Anchorage Road, Portsmouth, Hampshire, United Kingdom – PO35PU.

This work aims at three specific application areas. Firstly, the ground station that can handle multiple satellite signals at any given time as seen in Fig. 1. The increasing number of satellites in Lower-Earth Orbit (LEO) occupying Amateur Radio Spectrum together with variety of modulation techniques, data rates and protocols [9] used across the CubeSat community demands the integration of a multitude of communication standards onto a single platform. This is compounded by the problem of crowded spectrum [10] which is driving research on more efficient use of the available spectrum e.g., by de-confliction or Cognitive Radio (CR) techniques. For all such applications, a universal programmable hardware is desirable, which intensifies the interest in Software Defined Radio (SDR) in recent years [11]. Such an SDR must be robust in noisy and/or contested spectrum and make maximum use of a priori information to minimise initial acquisition and detection bandwidths.

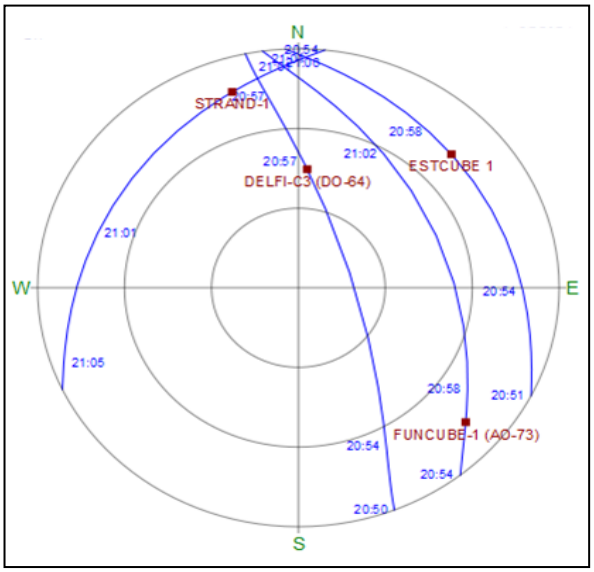

Fig. 1. Radar View of the Antenna Showing Different Satellites in Visibility

Secondly, the need for deployable mobile ground station network for the purposes of increased access time such as ESA's Global Educational Network for Satellite Operations (GENSO) system [12] and Satellite Networked Open Ground Station (SatNOGS) [13]. A ground station based on SDR hardware is suitable for worldwide distributed systems, where updates containing the software for communicating with new waveforms could be shared among different distant stations without the need for hardware upgrades.

Delta-sigma ADCs in a nutshell

Part one of a three-part series exploring the basic topology and functions of delta-sigma ADCs.
By Bonnie Baker -- EDN, 12/14/2007

Delta-sigma converters are ideal for converting signals over a wide range of frequencies from dc to several megahertz with very-high-resolution results. **Figure 1** shows the basic topology, or core, of a delta-sigma ADC, which has an internal delta-sigma modulator in series with a digital filter. As you explore delta-sigma ADCs, you will find that, although they have a variety of other features, they all possess this basic structure. This column and the next three *Baker's Best* columns explore the basic topology and functions of these two modules.

The input signal to the delta-sigma ADC is an ac or dc voltage. This and the next three *Baker's Best* columns use a single cycle of a sine wave as the input signal. Using a 1-bit internal ADC, the internal converter modulator in **Figure 1** samples the input signal, producing a coarse, quantized output. The modulator converts the analog-input signal into a high-speed, pulse-wave representation. The ratio of ones to zeros in the modulator's output pulse train mirrors the input-analog voltage. Although the modulator produces a noisy output, future columns will show that the circuit "shapes" this noise into the higher frequencies of the output spectrum. This action paves the way for a low-noise, high-resolution conversion at the output of the digital filter.

At the modulator output, the digital filter addresses high-frequency noise and high-speed-sample-rate issues. Because the signal now resides in the digital domain, you can apply a lowpass digital filter to attenuate the higher frequency noise and a decimator filter to slow down the output-data rate. The digital/decimator filter samples and filters the modulator's stream of 1-bit codes and creates a slower multibit code.

Although most converters have only one sample rate, delta-sigma converters have two: the input sampling rate and the output-data rate. The ratio of these two meaningful variables defines the system's decimation ratio. A strong relationship exists between the decimation ratio and the converter's effective resolution. A future column will examine how the modulator, digital/decimator filter, and adjustable decimation ratio work.

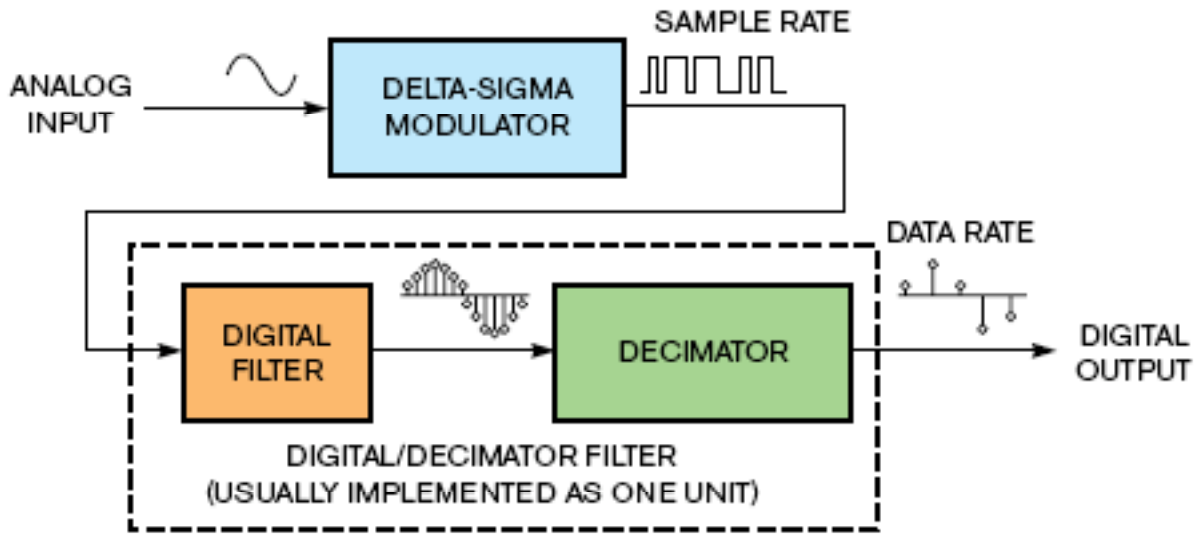

Figure 1 The core functions inside any delta-sigma ADC are a delta-sigma modulator and a digital/decimator filter.

Demonstration of focus-tunable diffractive Moiré-lenses

Stefan Bernet,* Walter Harm, and Monika Ritsch-Marte

Division for Biomedical Physics, Innsbruck Medical University, A-6020 Innsbruck, Austria

*stefan.bernet@i-med.ac.at

Abstract: In an earlier publication [Appl. Opt. **47**, 3722 (2008)] we suggested an adaptive optical lens, which consists of two cascaded diffractive optical elements (DOEs). Due to the Moiré-effect the combined optical element acts as a Fresnel zone lens with a refractive power that can be continuously adjusted by a mutual rotation of the two stacked DOEs. Here we present an experimental realization of this concept. Four designs of these Moiré-DOEs (MDOEs) were fabricated in thin (0.7 mm) glass slides by lithography and subsequent etching. Each element was realized as a 16 phase level DOE designed for 633 nm illumination. Our experimental investigation shows that the Moiré-lenses have a broad adjustable refractive power range with a high efficiency, which allows one to use them for flexible beam steering and for imaging applications.

OCIS codes: (050.1970) Diffractive optics; (120.3620) Lens system design; (090.1970) Diffractive optics.

References and links

1. L. Guoqiang, "Adaptive lens," Progress in Opt. **55**, 199–283 (2010).
2. H. Ren, S. Xu, Y.-J. Lin and S.-T. Wu, "Adaptive-focus lenses," Opt. Photon. News 43–47 Oct. 2008.
3. G. Zhou, H. M. Leung, H. Yu, A. S. Kumar, and F. S. Chau, "Liquid tunable diffractive-refractive hybrid lens," Opt. Lett **34**, 2793-2795 (2009).
4. T. Nose, and S. Sato, "A liquid crystal microlens obtained with a non-uniform electric field," Liq. Cryst. **5**, 1425-1433 (1989).
5. S. Xu, Y.-J. Lin, and S.-T. Wu, "Dielectric liquid microlens with well-shaped electrode," Opt. Express **17**, 10499 (2009).
6. H. Ren, D. Fox, B. Wu, and S. T. Wu, "Liquid crystal lens with large focal length tunability and low operating voltage," Opt. Express **15**, 11328-11335 (2007).
7. P. Valley, D. L. Mathine, M. R. Dodge, J. Schwiegerling, G. Peyman, and N. Peyghambarian, "Tunable-focus flat liquid-crystal diffractive lens," Opt. Lett. **35**, 336-338 (2010).
8. P. J. Valle, V. F. Canales, and M. P. Cagigal, "Focal modulation using rotating phase filters," Opt. Express **18**, 7820–7826 (2010).
9. S. Bernet and M. Ritsch-Marte, "Adjustable refractive power from diffractive Moiré elements," Appl. Opt. **47**, 3722–3730 (2008).
10. S. Bará, Z. Jaroszewicz, A. Kolodziejczyk, and V. Moreno, "Determination of basic grids for subtractive Moiré patterns," Appl. Opt. **30**, 1258–1262 (1991).
11. Z. Jaroszewicz, A. Kolodziejczyk, A. Mira, R. Henao, and S. Bará, "Equilateral hyperbolic moiré zone plates with variable focus obtained by rotations," Opt. Express **13**, 918-925 (2005).
12. J.M. Burch and D.C. Williams, "Varifocal Moiré zone plates for straightness measurement," Appl. Opt. **16**, 2445-2450 (1977).
13. A. W. Lohmann, "A new class of varifocal lenses," Appl. Opt. **9**, 1669–1671 (1970).
14. A. Kolodziejczyk and Z. Jaroszewicz, "Diffractive elements of variable optical power and high diffraction efficiency," Appl. Opt. **32**, 4317–4322 (1993).

#183108 - $15.00 USD Received 8 Jan 2013; revised 1 Mar 2013; accepted 1 Mar 2013; published 13 Mar 2013

An inexpensive hyperbolic positioning system for tracking wildlife using off-the-shelf hardware

SW Krüger

22036784

Dissertation submitted in fulfilment of the requirements for the degree Masters in Computer and Electronic Engineering at the Potchefstroom Campus of the North-West University

Supervisor: Prof ASJ Helberg

Co-supervisor: Dr PP Krüger

May 2017

Some Measurements on DVB-T Dongles with E4000 and R820T Tuners: Image Rejection, Internal Signals, Sensitivity, Overload, 1dB Compression, Intermodulation

August 2013
HB9AJG

Contents:

1. Motivation

After having read quite a few posts in the user group http://*uk.groups.yahoo.com/group/SDRSharp* about the sensitivity or "deafness" of these dongles, but not having come across any figures, I feel constrained to post the results of my tests. I have measured two types of dongles:

- a Terratec dongle, containing an E4000 tuner and the RTL2832,
  VID + PID = 0CCD 00D7, designated *E4000* further down.
- a "no name" dongle marked "DVB-T+DAB+FM ", containing an R820T tuner and the RTL2832,
  VID + PID = 0BDA 2838, designated *R820* further down.

2. Test Setup

Instruments used:
- HF Signal Generators HP8657A (0.1…1040MHz) and HP8640B (0.5…520MHz)
- AF Voltmeter HP333A.

Software used: SDR# v1.0.0.135
Settings:
- *Configure*: 2.048MSPS, RTL AGC off, Tuner AGC off, RF Gain max (49dB for the R820, 42dB for the E4000)
- *Radio*: CW-U, Bandwidth 500Hz, Filter Order 300
- *AGC* off
- *FFT Display*: Window Blackman-Harris, Resolution 262144.
- In the spectrum display the noise floor appears at about -40dBm. In order to display the levels of received signals closer to reality, in *SDRSharp.exe.Config* I modified the value -40.0 in line *<add key="fftOffset"value ="-40.0"* to *"-120.0"*.

Having been an HF engineer and a ham radio operator for over 40 years, I am used to measure receiver sensitivity in dBm. I am aware of those UHF enthusiasts who are used to rate their receivers by Noise Figure (NF). It is easy to go from dBm to NF, however, by using the formula:

NF = Power of the MDS (dBm) + 174dBm - 10log(Bandwidth) - Measured S/N.

Example:
MDS (Minimum Discernible Signal) = Signal giving an (S+N)/N of 3dB (measured with the AF Voltmeter).
10log(Bandwidth) in my measurements is 10log(500) = 27dB.
For (S+N)/N = 3dB, S is equal to N. Thus, S/N is 0dB.
So, for an MDS of, say, -140dBm: NF = -140 + 174 - 27 - 0 = 7dB.

Remark 1: The dongles have a nominal input impedance of 75 Ohms, whereas my signal generators have output impedances of 50 Ohms. My dBm figures take account of the difference of 1.6dB.

Remark 2: The measurements were carried out on one dongle of each type only. Of course, the results may vary by several dBs between individual dongles.

Remark 3: In such measurements uncertainties of +/-1…2dB are common.

Review of Inductive Pulsed Power Generators for Railguns

Oliver Liebfried

***Abstract*—This literature review addresses inductive pulsed power generators and their major components. Different inductive storage designs like solenoids, toroids and force-balanced coils are briefly presented and their advantages and disadvantages are mentioned. Special emphasis is given to inductive circuit topologies which have been investigated in railgun research such as the XRAM, meat grinder or pulse transformer topologies. One section deals with opening switches as they are indispensable for inductive storages and another one deals briefly with SMES for pulsed power applications. In the end, the most relevant inductor systems which were realized in respect to railgun research are summarized in a table, together with its main characteristics.**

***Index Terms*—Railgun, Pulsed power, review.**

I. Introduction

INDUCTIVE storages are used in pulsed power generators for railguns for several reasons. In combination with a homopolar generator (HPG) or a battery, inductors are used to generate the high voltage which is needed to inject current into a railgun at high armature velocities. They are used in capacitor banks to limit the maximum current amplitude and adjust the pulse length to the requirements of the railgun. Furthermore, they decouple several capacitor modules from each other and allow time-delayed switching and therefore pulse shaping. However, inductor research was not very evident within the electromagnetic launch community in the past as inductors were mostly part of HPG, capacitor bank, or battery system development. Thus, there is no comprehensive reference work about inductive storage systems for pulsed power generation. This paper aims at filling the gap as inductive pulsed power systems are becoming more relevant due to emerging technologies like Li-ion batteries, supercapacitors, and superconductors.

II. Inductive storage

Charged inductors can be seen as current sources which can create any voltage, assuming a corresponding insulation. Thus, inductors represent an ideal power source for railguns. In an inductive storage, energy is stored by its magnetic field. The interaction between the magnetic field and the current in the windings creates Lorentz forces on the windings of the inductor. Therefore, a coil can be regarded as a pressure vessel with the magnetic field B as a pressurized medium. The corresponding pressure p is related by $p = \frac{1}{2\mu}B^2$ to the magnetic field B with the permeability μ. The energy density of the inductor is directly linked to the magnetic field and therefore, its maximum depends on the tensile strength of the windings and the mechanical support. The upper limit for the energy density W/V follows from the virial theorem and can be expressed by

$$W/V = \lambda\sigma \tag{1}$$

where σ is the tensile strength of the coil material and λ is a coefficient related to the structural efficiency of the coil design [1], [2]. $\lambda = 1$ is the maximum value which is achievable by an ideal coil geometry. In the case of long and thin solenoidal coils or toroidal coils, λ gets close to $\frac{1}{3}$ [3], [4]. In practice, the best value for λ can be achieved with short solenoidal coils like the Brooks coil, where λ can be as high as $\frac{1}{2}$ [1], [4].

In superconducting coils, the mechanical stress is the major limitation of the energy density. In normal conducting coils, other limitations like resistive losses or heat dissipation might be more critical than the mechanical stress.

III. Superconducting magnetic energy storage

Ohmic losses can be avoided by using superconducting coils. In this case, the current could be stored for very long time periods. Instead of electrical losses, thermal losses of the cooling system have to be considered. The maximum energy and power of a superconducting coil is limited by the maximum breakdown voltage, the operating conditions of the conductor material and its mechanical strength [5]. Both the mechanical support and the electrical isolation will increase the coil volume and mass. Additionally, the cooling system has to be considerred. Therefore, superconducting coils for high-power applications are still very bulky. Nowadays, the realized superconducting magnetic energy storage (SMES) systems in the order of 1 MJ/1 MW have a volume exceeding $2\,\mathrm{m}^3$ (estimated from [6]). When the corresponding vacuum vessel, vacuum pumps and cooling equipment are taken into account, the volume can easily be multiplied by a factor of two or more. Therefore, a normal conducting coil seems presently more appropriate if a high energy density is desired.

However, several researchers applied superconducting coils in small scale demonstrators [7]–[10]. Some of them applied the superconductor itself as opening switch by letting it quench on purpose [11]–[13]. A 20 MJ/1 MA conceptional design for a high temperature superconducting coil pulsed power generator is presented in [14], [15].

IV. Coil design

The optimization of normal conducting coils with respect to the energy density and L/R is usually performed by optimizing the inductance per given piece of wire (GPW) [16]. The coil with the best inductance per GPW is known as the

O. Liebfried is with the French-German Research Institute of Saint-Louis (ISL), 5 rue Général Cassagnou, 68301 Saint-Louis, France, e-mail: Oliver.Liebfried@isl.eu.

Manuscript received Jan. 15, 2017; revised XXX XX, 2017.

A new metal-dielectric cathode with long lifetime

Ping Wu, Jun Sun, Guozhi Liu, Zhanfeng Yang, Shaofei Huo, and Wenyuan Liu

Citation: Physics of Plasmas **24**, 073104 (2017); doi: 10.1063/1.4990557
View online: http://dx.doi.org/10.1063/1.4990557
View Table of Contents: http://aip.scitation.org/toc/php/24/7
Published by the American Institute of Physics

A low-cost, Arduino-like development kit for single-element ultrasound imaging*

Luc Jonveaux[1]

***Abstract*— An open-source software ecosystem for ultrasound imaging is widely available to developers, however, limited resources can be found on the open-hardware side. The focus of this work was to develop an easy-to-use platform kit (hardware and software) for providing the community a complete experimental setup for ultrasound imaging at a low cost, without the need of specific equipment. The goal of this work resembles the needs of medical systems in the 80's where analog techniques using single-sensor devices were prominent.**

To this end, two open-source, arduino-like modules have been developed for building a simple, yet complete, single-channel analog front-end system, where all the intermediary signals are readily accessible by the user. A single-channel architecture avoids the beamforming overhead, though it limits the quality of the captured image, and brings simplicity to the system.

The modules were tested using re-purposed ultrasound mechanical probes, as well as non-medical transducers. Furthermore, different digital acquisition systems were utilized for providing the images of interest. The developed modules can also be used in Radio Frequency (RF) projects, non-destructive testing and control projects, as well as in low-cost medical imaging projects.

I. Introduction

A. Approach

Ultrasound imaging has evolved since the first ultrasound machine appeared. The first devices were using single-sensor (transducers) techniques, coupled with mechanical scanning [22]. The architecture of such systems, as shown in Fig. 1, is well-known and formed the basis of ultrasound imaging.

Mechanical scanning has its limitation, but also its strengths: a single signal channel, linked to a single sensor, means that the corresponding electronics are simplified, and the cost is reduced. Moreover, with progress made in different technical fields, mechanical probes are seen on the market again. Search in academic literature, and open-electronics resources, yielded little to no documentation of previous research to rebuild these mechanical ultrasound imaging devices.

To the best of the author's knowledge, there are no open-source hardware designs nor electronics accessible online for the analog-processing component. To bridge this gap, this work provides modules to the community to understand and recreate the electronic core of an ultrasound device.

B. This work

This kit consists of several modules mainly built from easily available components. **Two electronic modules were specifically designed to provide the basic development kit**. These two modules, called the Ultrasound Imaging Analog Core (UIAC), as shown in Fig. 1, are:

- the **Transducer Pulser Module (TPM)**: designed to provide a precise high-voltage pulse, necessary to excite the sensor, while remaining robust enough to be controlled by an Arduino;
- the **Analog Processing Module (APM)**: designed to correctly process the raw ultrasound electric signal, while easily exposing all intermediary signals, and exposing a digital output to the user.

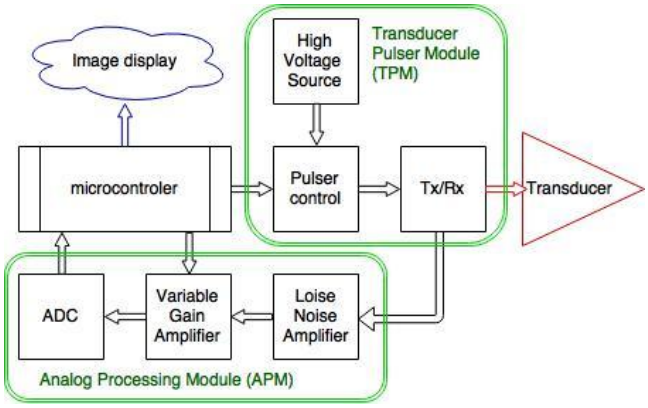

Fig. 1. Architecture of the ultrasound imaging system. The two custom boards, TPM and APM, are shown in green.

C. A module approach

We have chosen a modular approach to ensure that each key component inside the ultrasound image processing can easily be replaced and compared with another module. Each electronic module takes the place of a function in the signal processing chain or allows tapping into the different signals circulating between the blocks.

We have considered readily available open-source modules and recycled components (probes) to provide the user with building bricks for the basic non-medical ultrasound imaging tool.

We remind that the aim of this work is not to design an ultrasound probe: *the goal of the present article is rather to provide a basic open-source tool to understand ultrasound imaging technique and provide the analog core, unavailable today, as well as selecting proper off-the-shelf components for the other elements*.

This paper also discusses several possible options, keeping in mind that none are preferred and that the modular

*This work was not supported by any organization

[1]Luc is just a independant maker, reachable at kelu124 at gmail.com

Microwave Transistor Amplifiers

Analysis and Design

Second Edition

Guillermo Gonzalez

In vivo magnetic recording of neuronal activity

Laure Caruso[1], Thomas Wunderle[2], Christopher Murphy Lewis[2], Joao Valadeiro[3,4], Vincent Trauchessec[1], Josué Trejo Rosillo[1], José Pedro Amaral[3,4], Jianguang Ni[2], Patrick Jendritza[2], Claude Fermon[1], Susana Cardoso[3,4], Paulo Peixeiro Freitas[3,4], Pascal Fries[2,5,6,*], Myriam Pannetier-Lecoeur[1,6,7,*]

[1]SPEC, CEA, CNRS, Université Paris-Saclay, CEA Saclay 91191 Gif-sur-Yvette Cedex, France.
[2]Ernst Strüngmann Institute (ESI) for Neuroscience in Cooperation with Max Planck Society, Deutschordenstraße 46, 60528 Frankfurt, Germany.
[3]Instituto de Engenharia de Sistemas de Computadores-Microsystems and Nanotechnology (INESC-MN), Rua Alves Redol, No. 9, Lisboa 1000-029, Portugal.
[4]Instituto Superior Técnico IST, Physics Department, Universidade de Lisboa, Lisbon 1049-001, Portugal.
[5]Donders Institute for Brain, Cognition and Behaviour, Kapittelweg 29, 6525 EN Nijmegen, Netherlands.
[6]These authors contributed equally.
[7]Lead contact.
*Correspondence: myriam.lecoeur@cea.fr, pascal.fries@esi-frankfurt.de

KEYWORDS

Magnetic fields, magnetoencephalography, MEG, spin electronics, magnetic sensors.